

SYNTHETIC LISA: SIMULATING TIME DELAY INTERFEROMETRY IN A MODEL LISA

MICHELE VALLISNERI

Jet Propulsion Laboratory, California Institute of Technology, Pasadena, CA 91109

July 26, 2004

ABSTRACT

Synthetic LISA, developed at the Jet Propulsion Laboratory, is a C++/Python package to simulate the LISA science process at the level of scientific and technical requirements. It generates synthetic time series of the LISA fundamental noises, as filtered through all the Time-Delay-Interferometric (TDI) observables; it provides a streamlined module to compute the TDI responses to gravitational waves, according to a full model of TDI (including the motion of the LISA array, and the temporal and directional dependence of the arm lengths). *Synthetic LISA* is written as a C++ modular package that allows adding code for specific gravitational-wave sources, or for new noise models; time series for waves and noises can also be easily loaded from disk or memory. In this paper we describe the theoretical model that underlies *Synthetic LISA*, we discuss the implementation of the package, we test its correctness, and we show examples of its use in characterizing the laser-noise residuals left by first-generation TDI with realistic time-dependent arm lengths, and in estimating the arm length-measurements error budgets required for effective laser-noise cancellation in both first- and second-generation TDI.

Subject headings: gravitation — gravitational waves — instrumentation: interferometers — space vehicles

1. INTRODUCTION TO SYNTHETIC LISA

The Laser Interferometer Space Antenna (LISA) is a joint NASA-ESA deep-space mission aimed at detecting and studying gravitational radiation in the 10^{-5} – 10^{-1} Hz frequency band (LISA Study Team 1998). It is expected to be launched in the year 2012, and to start collecting scientific data approximately a year later, after reaching its final orbital configuration (Folkner et al. 1997). LISA consists of three widely separated spacecraft flying in a triangular, almost equilateral configuration, and exchanging coherent laser beams; gravitational waves (GWs) will be measured by picometer interferometry as modulations in the distance between the spacecraft. LISA holds the promise of providing access to entirely new classes of GW sources, but it also introduces complications unknown to ground-based detectors, such as the complex signal and noise transfer functions, the problem of canceling the otherwise overwhelming laser phase noise, the necessity of dealing simultaneously with many continuous signals (including a confusion-noise background of galactic white-dwarf binaries), and the possibility of using multiple interferometric observables as a network of GW interferometers.

These complications hinder the analytical characterization of LISA’s detection capabilities as a function of its configuration, as well as the development of data analysis techniques aimed at specific GW sources. Computer simulations will therefore play a crucial role in exploring LISA’s performance and in obtaining insight about its optimal operation. In this paper we report about *Synthetic LISA*, a software package that we developed to simulate the LISA science process at the interface of scientific and technical mission requirements. *Synthetic LISA* is released as public-domain software, available for

download from the *Open Channel Foundation*.¹

Because we aim to explore the interface between science and technology, our package operates at a higher level than integrated-modeling simulations (Merkowitz 2003; Merkowitz et al. 2004) – we do not model space-craft subsystems, but rather we assume nominal specifications of their performance – but at a lower level than simulations oriented mainly to data-analysis (Cornish & Rubbo 2003) – we perform an explicit time-domain simulation of interferometry, including the cancellation of laser phase noise. *Synthetic LISA* produces synthetic time series of the LISA fundamental noises and of the LISA response to GWs, useful for (among other things):

Performance characterization and architecture trade-off studies. Synthetic time series supplement analytical results in the allocation of subsystem noise budgets and in the determination of the final sensitivity for specific GW sources, providing a high-level analysis tool for system engineering, and helping the formulation of technical requirements from the desired LISA science goals.

Noise analysis and vetos. Synthetic time series can be used to study real-LISA features of the instrumental noises, such as nonstationarity, noise increments due to faulty subsystems, or (perhaps most important) the level of cancellation of laser phase noise by Time-Delay Interferometry (TDI; see Sec. 2) under different LISA geometries, arm length-measurement tolerances, and TDI implementations.

Optimal combination of the LISA data, and verification of sensitivity. Achieving LISA’s optimal sen-

¹ Open Channel Foundation: www.openchannelfoundation.org; for *Synthetic LISA* information and updates, see also www.vallis.org/syntheticlisa.

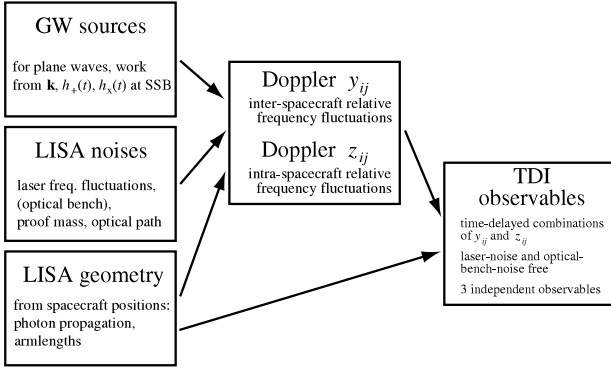


FIG. 1.— A block diagram of the LISA science process.

sitivity requires using all the interferometric observables of the array together (Prince et al. 2002). Synthetic data can be used to supplement analytic results for the optimal combinations under simulated conditions that model potential real-LISA effects such as the nonstationarity of noises, the presence of data gaps, and so on.

Development of data-analysis algorithms. The synthetic time series produced by this simulation have consistent signal structure and noise correlations across all the TDI combinations. Thus they can be used to test algorithms for use on the real LISA data, such as the separation of stochastic GW backgrounds from LISA instrumental noises (Tinto et al. 2000; Hogan & Bender 2001), the matched-filtering detection of quasiperiodic signals (Królak et al. 2004), and so on. *Synthetic LISA* provides a streamlined module to filter GWs through the LISA TDI response, allowing easy interfacing to existing GW data or GW-modeling applications.

Synthetic LISA represents the evolution of previous simulation tools used within the LISA project. Among the improvements to the simulator tool described by Vallisneri & Armstrong (2003), *Synthetic LISA* is based on a full model of TDI: the LISA arm lengths are changing realistically with the motion of the array (in the previous simulator they were fixed to integer multiples of the simulation timestep); the laser beams propagate causally (i.e., are subject to aberration, again due to the motion of the array); and the full set of TDI combinations can be generated (including *second-generation* observables that cancel laser noise in the case of a shearing noise array).

This paper is laid out as follows. In Sec. 2 we describe the theoretical model of the LISA science process used in the simulation; in Sec. 3 we discuss the implementation and usage of *Synthetic LISA*; in Sec. 4 we test the package and show some examples of its application; in Sec. 5 we give our conclusions. In the following, we set $G = c = 1$ unless otherwise indicated.

2. MODELING OF A SYNTHETIC LISA

Figure 1 is a block diagram of the LISA science process, as modeled in *Synthetic LISA*. At the top of the hierarchy sit the TDI observables, which represent the main scientific product of the mission, and which will be run through data-analysis algorithms to search for GW signals. The TDI observables are time-delayed com-

bination of the basic interferometric measurements (y and z) that compare the frequencies (or phases) of the two lasers on each spacecraft between themselves, and with the lasers incoming from the other two spacecraft. The Doppler measurements bear the imprint of the instrumental noises and of the GW signals, but the latter can be read off efficiently only from the TDI observables, which are free of the otherwise overwhelming laser phase noise and optical-bench noise. The time-dependent geometry of laser propagation across the LISA array influences the effect of the LISA noises and (especially) of GW signals on the Doppler measurements; a precise knowledge of geometry is needed also to build the TDI observables in such a way that laser phase noise and optical-bench noise are canceled effectively. In this section we go through all the elements of Fig. 1, and discuss in detail how they are modeled in *Synthetic LISA*. In Sec. 2.1 we describe the geometry of the LISA array, and the setup of the interferometric payload on each spacecraft; in Secs. 2.2 and 2.3 we describe the response of the basic interferometric observables to GWs and to the LISA fundamental noises; last, in Sec. 2.4 we give a rapid overview of TDI as used in LISA.

2.1. LISA geometry and interferometry

The motion of the LISA array is complex: at the qualitative level, the three LISA spacecraft maintain a quasi-equilateral triangular configuration (where the arms stay equal to about 1%) orbiting the Sun once per year at an orbital separation of one AU, trailing the Earth along its orbit in the plane of the ecliptic; at the same time, the constellation maintains an inclination of $\pi/2 - \pi/6 = \pi/3$ with respect to the plane of the ecliptic (as measured from the normal of the instantaneous plane of the LISA constellation to the normal to the plane of the ecliptic), and it performs a cartwheeling motion, rotating around the normal to the instantaneous LISA plane with a rotation period of a year. This picture is realized in practice by placing the three spacecraft on eccentric, inclined solar orbits (Folkner et al. 1997).

This pattern of motion improves the sensitivity of LISA to GW signals, making it more homogeneous over the sky (because the dependence of the antenna patterns to source position is averaged during the year), and improving the estimation of source position and polarization (because the GW responses become modulated by the variation of the antenna patterns). This added sensitivity comes at the price of complicating the GW response: the modulations induced by the changing orientation of the LISA plane spread the power of originally monochromatic GW signals, generating several sidebands at frequency multiples of 1/yr (LISA Study Team 1998; Cornish & Larson 2003; Królak et al. 2004); furthermore, the relative motion of the detector with respect to the GW source introduces a time-dependent Doppler shift, which is the dominant effect for signals above 10^{-3} Hz [the characteristic bandwidth of the Doppler shifting is $\sim (\Omega R/c)f$, where f is the GW frequency].

When LISA is in operation, each spacecraft will exchange laser beams with the other two, measuring the phase of the arriving laser beams with respect to the local lasers; the laser beams are bounced off freely-falling proof masses that are shielded by the spacecraft

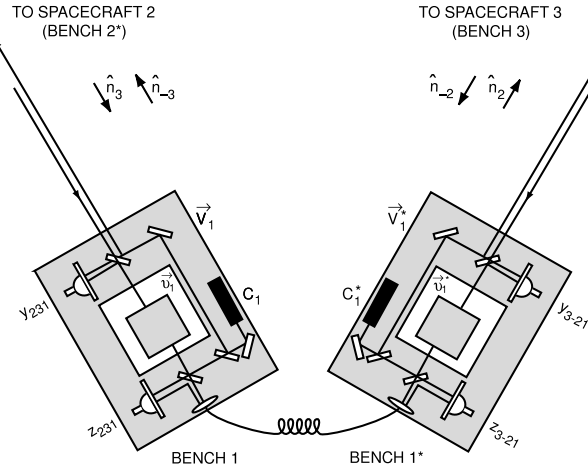


FIG. 2.— Schematic diagram of the proof-mass and optical-bench assemblies within each LISA spacecraft [adapted from Peterseim et al. (2000)].

from most external disturbances,² so that they can serve as references for the measurement of GWs. To implement this measurement scheme, each spacecraft will carry two lasers, two proof masses, and two optical-readout schemes. Figure 2 presents a schematic diagram [adapted from Peterseim et al. (2000)] of the proof-mass and optical-bench assemblies within one of the LISA spacecraft, labeled “1”; the other two spacecraft have identical setups. In short:

1. the left-hand bench receives the laser beam from spacecraft 2, bounces it off its proof mass, and compares it with the local laser (without bouncing the latter) at the upper photodetector;
2. via an optical fiber, the left-hand bench receives the right-hand-bench laser and compares it with the local laser (without bouncing the latter) at the lower photodetector;
3. the left bench sends out the local laser (without bouncing it) to spacecraft 2, and (after bouncing it off the other side of its proof mass) to the right-hand bench.

The operation of the right-hand bench (and indeed, of the benches on the other two spacecraft) is similar. [A recent redesign of the optical benches (B. L. Schumaker 2004, private communication) would implement the comparison of the two lasers on the two benches of the same spacecraft by measuring their phases separately, doing away with the optical fiber, and then subtracting the measurements. For the purpose of obtaining the laser-noise-free TDI signals (see Sec. 2.4) this modification amounts only to a redefinitions of the z_{slr} measurements (J. W. Armstrong, F. B. Estabrook, & M. Tinto 2004, private communication), so in this paper, and indeed in *Synthetic LISA*, we refer to the older architecture.]

In this setup, the physical observable of interest is the comparison of phase between the local laser and the in-

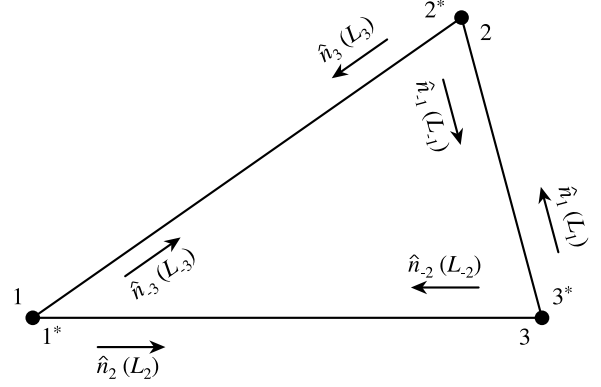


FIG. 3.— Schematic LISA configuration. The spacecraft are labeled 1, 2, and 3; each spacecraft contains two optical benches, denoted by 1, 1*, 2, 2*, 3*, as indicated. The unit vectors \hat{n}_l and light-path lengths L_l connecting spacecraft s and r are indexed by $l = \{1, 2, 3\}$ for $(s, r) = \{(3, 2), (1, 3), (2, 1)\}$, and $l = \{-1, -2, -3\}$ for $(s, r) = \{(2, 3), (3, 1), (1, 2)\}$.

coming laser, which carries information about the variations induced by GWs in the inter-spacecraft optical path. The phase fluctuations of the lasers, however, are generally much larger than the GW-induced phase shifts, and must be subtracted before GWs can be resolved. In the last few years, a number of authors collaborated to develop a scheme (*Time-Delay Interferometry*, or TDI) to subtract laser noise by carefully combining time-shifted series of the inter- and intra-spacecraft phase measurements; if the lasers are not phase-locked to a master (see the end of Sec. 2.4), the intra-spacecraft phase measurements carry no information about GWs, but they do carry a combination of the phase noises from the lasers within each spacecraft.

Because TDI has its origin in the techniques used to measure GWs by the Doppler tracking of distant spacecraft (Estabrook & Wahlquist 1975; Wahlquist 1987; Armstrong et al. 1987; Bertotti et al. 1995; Tinto 2002; Armstrong et al. 2003b), it prefers to describe the comparisons between laser beams in terms of fractional frequency differences rather than relative phase shifts [the two descriptions are exactly equivalent (Tinto et al. 2002), as they are related by time integration]. Thus, TDI represents the LISA readouts as *basic Doppler observables*: $y_{slr}(t)$ is the fractional frequency difference at time t between the beam received at spacecraft r (eceiver) from spacecraft s (ender) and the local laser; and $z_{slr}(t)$ is the analogous intra-spacecraft measurement *on the same optical bench* (thus, although it carries the index s it is in fact the fractional frequency difference between the two lasers of spacecraft r). In this paper, the index l (ink) denotes the (oriented) LISA arm along which the laser was transmitted, according to the cyclical indexing $l = \{1, 2, 3\}$ for $(s, r) = \{(3, 2), (1, 3), (2, 1)\}$, and $l = \{-1, -2, -3\}$ for $(s, r) = \{(2, 3), (3, 1), (1, 2)\}$ (thus, $\text{sgn}(l) = \epsilon_{s|l|r}$). This spacecraft and link indexing is shown also in Fig. 3. Note that our notation for the basic Doppler observables merges the two notations used in the scientific literature on *first-generation* TDI (y_{lr} and z_{lr}) and, more recently, on *second-generation* TDI (y_{sr} and z_{sr}). Table 1 shows a comparison (as it were, a Rosetta stone) of the notations used in various papers on

² For instance, the spacecraft will not shield the proof masses from cosmic rays.

TDI. In the next two sections we discuss the response of these basic Doppler observables to GWs and to the noise sources present within each spacecraft.

2.2. LISA response to gravitational waves

In this section we give an expression for the GW response of the basic Doppler observables $y_{ij}(t)$. Working in an inertial reference frame filled by a plane GW with propagation vector \vec{k} and transverse-traceless gravitational tensor $\mathbf{h}(\vec{x}; t) = \mathbf{h}(0, t - \vec{k} \cdot \vec{x}) \equiv \mathbf{h}(t)$, we denote the positions of the three spacecraft by $\vec{p}_i(t)$. Following Estabrook & Wahlquist (1975) and Wahlquist (1987), we write the response of the inter-spacecraft LISA Doppler observable $y_{slr}(t)$ to the plane wave as

$$y_{slr}^{\text{gw}}(t) = [1 + \hat{k} \cdot \hat{n}_l(t)] \times (\Psi_l[t_{\text{send}} - \hat{k} \cdot \vec{p}_s(t_{\text{send}})] - \Psi_l[t - \hat{k} \cdot \vec{p}_r(t)]), \quad (1)$$

where t_{send} and $\vec{p}_s(t_{\text{send}})$ are determined by the light-propagation equation $t_{\text{send}} = t - |\vec{p}_r(t) - \vec{p}_s(t_{\text{send}})|$, where $\hat{n}_l(t)$ is the oriented photon-propagation unit vector $\hat{n}_l(t) \propto \vec{p}_r(t) - \vec{p}_s(t_{\text{send}})$, and where

$$\Psi_l(t') = \frac{\hat{n}_l(t) \cdot \mathbf{h}(t') \cdot \hat{n}_l(t)}{2(1 - [\hat{k} \cdot \hat{n}_l(t)]^2)}. \quad (2)$$

Equation (1) gives the inter-spacecraft Doppler observable for laser-beam reception at time t on spacecraft r from spacecraft s , through link l . The two $\hat{k} \cdot \vec{p}$ products correspond to the retardation of the plane wavefront to the position of the two spacecraft, while the $\hat{k} \cdot \hat{n}$ products come in as geometrical projection factors (Estabrook & Wahlquist 1975; Wahlquist 1987). Equation (1) is not singular for $\hat{k} = \pm \hat{n}_l$, because in that case the transverse-traceless tensor \mathbf{h} is orthogonal to \hat{k} and \hat{n}_l , and the Ψ_l go to zero.

The light-propagation equation defines the effective armlength $L_l(t)$ experienced by light propagating from s to r , for reception at time t :

$$L_l(t) = |\vec{p}_r(t) - \vec{p}_s(t - L_l(t))|. \quad (3)$$

Note that in general $L_l(t) \neq L_{-l}(t)$.

The response to GWs of the intra-spacecraft Doppler observable $z_{slr}(t)$ is null, because the distance traveled by the intra-spacecraft beam is negligible for the GW amplitudes and wavelengths relevant to LISA.³

2.3. LISA response to fundamental noises

In this section we give the response of the basic Doppler observables to the fundamental noise sources present within each spacecraft. Looking back to Fig. 2, we label the left-hand and right-hand optical benches (and their lasers) as 1 and 1^* , respectively (more generally, unstarred benches transmit into oriented arms with negative indices). Following Estabrook et al. (2000), we denote the fractional frequency fluctuations of the laser on optical bench 1 as $C_1(t)$; these enter additively in the y_{231} measurement, together with the frequency noise from the laser on bench 2^* of spacecraft 2, retarded to the time of emission:

$$y_{231}^{\text{noise}}(t) = C_2^*(t - L_3(t)) - C_1(t) + \dots; \quad (4)$$

³ If the lasers are not phase-locked to a master (see the end of Sec. 2.4).

next, the y_{231} measurement is subject to noise due to fluctuations on the optical path of the beam incoming from spacecraft 2 (a combination of shot noise, pointing noise, and other optical-path noises), which we denote as y_{231}^{op} ; also, the velocity noise \vec{v}_1 of the proof mass on optical bench 1 (i.e., its deviation from perfect free fall) induces an additional Doppler shift on the incoming beam (the local beam does not bring in any velocity noise, since it is not bounced on the local proof mass):

$$y_{231}^{\text{noise}}(t) = C_2^*(t - L_3(t)) - C_1(t) + y_{231}^{\text{op}}(t) - 2\vec{v}_1(t) \cdot \hat{n}_3(t) + \dots; \quad (5)$$

last, the random velocities V_2^* and V_1 of the emitting and receiving optical benches (which are several orders of magnitude greater than \vec{v}_1) induce additional Doppler shifts with the same temporal structure of laser frequency noise:

$$y_{231}^{\text{noise}}(t) = C_2^*(t - L_3(t)) - C_1(t) + y_{231}^{\text{op}}(t) - 2\vec{v}_1(t) \cdot \hat{n}_3(t) + \vec{V}_2^*(t - L_3(t)) \cdot \hat{n}_3(t) - \vec{V}_1(t) \cdot \hat{n}_{-3}(t). \quad (6)$$

Along similar lines we derive the noise response of the intra-spacecraft measurement z_{3-21} on spacecraft 1, which contains the frequency noises from lasers 1 and 1^* at time t , the random velocities of the optical bench 1 and of its proof mass, and the frequency shift η_1 upon transmission through the optical fiber (ultimately due to a component of the relative bench motions, $\vec{V}_1 - \vec{V}_1^*$):

$$z_{3-21}^{\text{noise}}(t) = C_1(t) - C_1^*(t) + 2\hat{n}_3(t) \cdot \vec{v}_1 + 2\hat{n}_{-3}(t) \cdot \vec{V}_1 + \eta_1; \quad (7)$$

here we are ignoring time-delay effects along the fibers.

Throughout the rest of this paper (and indeed, always in *Synthetic LISA*) we take the optical-fiber noises and the optical-bench motions to be negligible. In fact, optical-fiber noise is removed in TDI by always using the z_{slr} observables in pairs such as $(z_{231} - z_{3-21})/2$, $(z_{312} - z_{1-32})/2$, and so on. One sees also that the optical-bench motions along the lines of sight (e.g., $\hat{n}_{-3} \cdot \vec{V}_1$, $\hat{n}_2 \cdot \vec{V}_1^*$, and $\hat{n}_3 \cdot \vec{V}_2^*$) can be absorbed in the corresponding laser frequency noise variables (e.g., C_1 , C_1^* , and C_2^*), because they appear in y_{slr}^{noise} and z_{slr}^{noise} with the same indices and the same evaluation times. Thus, if the TDI observables can successfully subtract laser frequency noise, they will also subtract the optical-bench motions, which are generally several orders of magnitude smaller.

In writing Eqs. (1), (6), and (7), we have neglected also the offsets (up to several hundred MHz) between the center frequencies of the six LISA lasers, as well as the slow Doppler drifts resulting from the relative motion of the spacecraft (up to tens of MHz). In practice, the frequency offsets and Doppler drifts will be corrected by down-converting the photodetector output and tracking fringe rates using onboard ultrastable oscillators (USOs) (Tinto et al. 2002, 2003). Although USOs introduce an important additional source of phase noise, their treatment is cumbersome, and we leave their modeling to a future version of *Synthetic LISA*.

Under these assumptions, the simulation of the LISA noise response requires time series for 18 fundamental noise variables: the six proof-mass velocity noises along the line of sight (which we denote as $pm_1 \equiv \hat{n}_3 \cdot \vec{v}_1$,

TABLE 1
A COMPARISON OF THE PHASE-MEASUREMENT AND LISA GEOMETRY CONVENTIONS USED IN THE LITERATURE ON TDI.

reference	geometry	inter-spacecraft measurement	intra-spacecraft measurement (on same bench of y with same indexes)	link vectors	armlengths
this paper		y_{slr} (frequency)	z_{slr}	n_l ($l > 0$ ccw, $l < 0$ cw)	L_l ($l > 0$ ccw, $l < 0$ cw)
AET 1999			n/a		
TAE 2000, ETA 2000, AET 2001, Hogan & Bender 2001, Prince et al. 2002, TEA 2002b AET 2003		y_{llr} (frequency)	z_{llr}	n_{ll} (along ccw)	L_{ll} (no distinction between ccw and cw)
TEA 2002, Tinto et al. 2003		s_{llr} (phase)	τ_{llr} (phase)		
Dhurandhar et al. 2002		$U_1 = y_{3-21}$, $U_2 = y_{1-23}$ $U_3 = y_{2-13}$, $V_1 = -y_{231}$ $V_2 = -y_{312}$, $V_3 = -y_{123}$	n/a	n_{ll} (along ccw)	L_{ll} (no distinction between ccw and cw)
Cornish & Rubbo 2003	$1 \rightarrow 2 \rightarrow 3$ ccw	Φ_{sr} (phase)	n/a	$r_{sr} = n_{sr}$	L_{sr} (oriented)
Cornish & Hellings 2003		y_{sr} (frequency)	n/a	n/a	
Królak et al. 2004			n/a	n_{ll} (along ccw)	L (equal arms)
Shaddock et al. 2003 ^a , TEA 2004 ^b	$1 \rightarrow 2 \rightarrow 3$ cw	s_{sr} (phase)	τ_{sr} (phase)	n/a	$L_{ll} = L_{-l}$, $L_{ll} = L_l$ (unprimed cw, primed ccw)
Shaddock 2004					L_{sr} (oriented)

In the cited references, A, E, and T refer to J. W. Armstrong, F. B. Estabrook, and M. Tinto. Notations are described with respect to the usage of this paper, with s \equiv sending spacecraft, l \equiv armlink, r \equiv receiving spacecraft; “cw” and “ccw” refer to the progression of spacecraft or link indexes, as seen when looking at the LISA constellation from above (from ecliptic latitude 90° N); when indexes are shown in absolute values, only positive values are used. Tinto and Armstrong 1999 (not included in this table) has $y_1 \equiv$ two-way ccw ($a \rightarrow b \rightarrow a$), $y_2 \equiv$ two-way cw ($a \rightarrow c \rightarrow a$).

^a The semicolon ordered-delay notation was introduced in Shaddock et al. 2003 and TEA 2004.

^b TEA 2004 uses $n_{|l|}$ to denote link vectors; it is ambiguous from the context whether these are ccw or cw.

$pm_2 \equiv \hat{n}_1 \cdot \vec{v}_2$, $pm_3 \equiv \hat{n}_2 \cdot \vec{v}_3$, and $pm_1^* \equiv \hat{n}_{-2} \cdot \vec{v}_1^*$, $pm_2^* \equiv \hat{n}_{-3} \cdot \vec{v}_2^*$, $pm_3^* \equiv \hat{n}_{-1} \cdot \vec{v}_3^*$), the six optical-path noises y_{slr}^{op} , and the six laser noises C_i and C_i^* . [Note that our definition of the pm_r^* differs by a factor -1 from

the definition used by Vallisneri & Armstrong (2003).]

The general expressions for y_{slr}^{noise} and z_{slr}^{noise} then become

$$y_{slr}^{\text{noise}}(t) = \begin{cases} C_s^*(t - L_l(t)) - C_r(t) + y_{slr}^{\text{op}}(t) - 2pm_r(t) & \text{if } l > 0, \\ C_s(t - L_l(t)) - C_r^*(t) + y_{slr}^{\text{op}}(t) - 2pm_r^*(t) & \text{if } l < 0, \end{cases} \quad (8)$$

and

$$z_{slr}^{\text{noise}}(t) = \begin{cases} C_r^*(t) - C_r(t) + 2pm_r^*(t) & \text{if } l > 0, \\ C_r(t) - C_r^*(t) + 2pm_r(t) & \text{if } l < 0. \end{cases} \quad (9)$$

We set standard levels for the 18 fundamental noises according to the noise budget discussed in the LISA pre-phase A report (LISA Study Team 1998). Note however that *Synthetic LISA* allows all these prescriptions to be overridden.

Laser Frequency Noise. We take each laser noise to be white, and to have a one-sided (square-root) spectral density of 30 Hz/√Hz, which converts to a power spectrum of fractional frequency fluctuations by squaring and dividing by the square of the optical frequency $\simeq c/(1064 \text{ nm}) = 2.82 \times 10^{14} \text{ Hz}$; thus, $S_n^{\text{ls}} = 1.1 \times 10^{-26} \text{ Hz}^{-1}$. We assume that the six laser noises are sta-

tistically independent (the lasers need not be locked).

Proof-Mass Noise. We take each proof mass to have white acceleration noise along the line of sight, with a one-sided (square-root) spectral density of $3 \times 10^{-15} \text{ m s}^{-2} \text{ Hz}^{-1/2}$, which converts to a power spectrum of fractional frequency fluctuations (Estabrook et al. 2000; Tinto et al. 2002b) by using the derivative theorem for Fourier transforms, and dividing by c^2 ; thus, $S_n^{\text{pm}} = (3 \times 10^{-15} \text{ m s}^{-2} \text{ Hz}^{-1/2})^2 / (4\pi^2 f^2 c^2) = 2.5 \times 10^{-48} [f/\text{Hz}]^{-2} \text{ Hz}^{-1}$. We assume that the six proof-mass noises are statistically independent.

Optical-Path Noise. We combine shot noise and

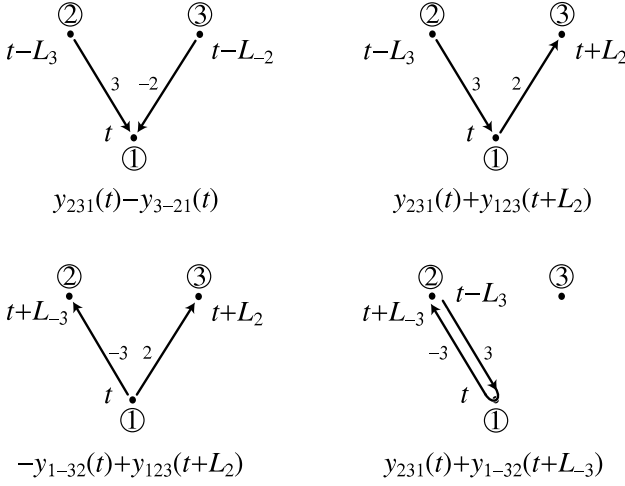


FIG. 4.— The four combinations of two basic Doppler observables with emission or reception at spacecraft 1 and at time t .

beam-pointing noise on each optical bench into aggregate optical-path noises; we take these to be white displacement noises, with a one-sided (square-root) spectral density of 20×10^{-12} m Hz $^{-1/2}$, which converts to a power spectrum of fractional frequency fluctuations by using the derivative theorem for the Fourier transform, and dividing by c^2 ; thus, $S_n^{\text{op}} = (20 \times 10^{-12}$ m Hz $^{-1/2})^2 \times (4\pi^2 f^2)/c^2 = 1.8 \times 10^{-37}$ [f/Hz] 2 Hz $^{-1}$. If the length of the LISA arms is different from the nominal value of 16.6782 s, we scale the optical-path rms noise by $L_l/(16.6782 \text{ s})$ to account for the $1/L_l^2$ power loss along the arms.⁴ We assume that our aggregate optical-path noise enters the y_{slr} and z_{slr} observables in the same way as shot noise, and we further assume that the six optical-path noises are statistically independent.

2.4. LISA TDI observables

Time	Delay	Interferometry	(TDI)
(Tinto & Armstrong 1999; Estabrook et al. 1999; Hogan & Bender 2001; Tinto et al. 2002; Tinto et al. 2003; Tinto et al. 2003; Cornish & Hellings 2003;	1999; 2000; 2001; 2002; 2002b; Armstrong et al. 2003; Cornish & Hellings 2003;	1999; 2000; 2001; 2002; 2002b; Armstrong et al. 2003; Cornish & Hellings 2003;	

⁴ The variance of shot noise is inversely proportional to the number of photons received, which is proportional to the power received. Since power scales as $1/L_l^2$, rms shot noise must scale as

Shaddock et al. 2003; Shaddock 2004; Tinto et al. 2004) is a technique to combine the basic Doppler variables y_{slr} and z_{slr} into composite observables that are sensitive to GWs, but that are free of the otherwise overwhelming laser frequency noise (they are also free of optical-bench and fiber noise, as discussed above). To understand how TDI works, it is useful to tie the algebraic representation of the TDI observables to a visual picture of the path traveled by light between the LISA spacecraft. Looking at Fig. 4, let us consider the four combinations $y_{231}(t) - y_{3-21}(t)$, $y_{231}(t) + y_{123}(t+L_2)$, $-y_{1-32}(t) + y_{123}(t+L_2)$, and $y_{231}(t) + y_{1-32}(t+L_3)$; the two laser beams involved in each of these combinations are either arriving to spacecraft 1 or leaving it at the time t ; the retardations by the armlengths L_2 and L_3 are needed because the Doppler observables are always labeled by the time of beam *reception*. Using Eq. (8), we see that for the first three combinations the contribution to laser frequency noise that is produced at time t is due to lasers 1 and 1^* , and it is equal to $-C_1(t) + C_1^*(t)$. In the fourth combination, $y_{231}(t) + y_{1-32}(t+L_3)$, no laser noise is produced at time t , because the same laser is used as emitter and reference. For the first three combinations, the laser-noise contribution *can be canceled* by subtracting from the y_{slr} expressions given above the intra-spacecraft measurement $(1/2)[z_{231}(t) - z_{3-21}(t)]$, whose laser-noise component is again $-C_1(t) + C_1^*(t)$ (in fact, as noted above, each of $z_{231}(t)$ and $-z_{3-21}(t)$ contains the combination $-C_1(t) + C_1^*(t)$, but the difference of the two z has the added advantage of canceling optical-fiber noise).

Naturally, the laser noise that is produced at the times $t-L_3$, $t-L_2$, $t+L_2$, and $t+L_3$ (in various combinations for the four y_{slr} expressions) is still not canceled. We see, however, that a combination of y_{slr} observables that corresponds graphically to a *closed circuit* would cancel laser noise completely; to build such a combination, we need to delay the times of evaluation for the y_{slr} so that the tip or tail of each arrow meets another tip or tail (and only one!) at just the right time. A simple example, valid in the case when the L_l are time-independent and all equal to L , traces a light path analogous to the path used in a Michelson interferometer (see the left panel of Fig. 5),

L_l . We assume that the remaining part of the aggregate optical-path noise scales in the same fashion.

$$[y_{123}(t+L_2) + y_{3-21}(t+L_2+L_{-2})] - [y_{1-32}(t+L_{-3}) + y_{231}(t+L_{-3}+L_3)] - \frac{1}{2}(z_{231}(t) - z_{3-21}(t)) + \frac{1}{2}(z_{231}(t+L_{-3}+L_3) - z_{3-21}(t+L_2+L_{-2})), \quad (10)$$

where the two interfering light beams leave spacecraft 1 at time t , and return at time $t+2L$. The two double- z_{slr} subtraction terms are needed for the initial time of emission of the two beams, and for the final time of

while laser noise is self-canceling at the zero-angle corners where the beams retrace their path, as mentioned above. Reordering Eq. (10) so that t is the final time of

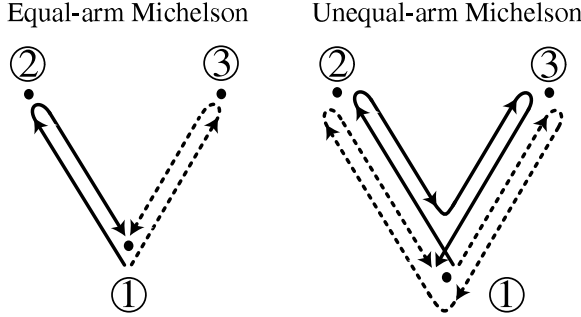


FIG. 5.— Tracing the light paths in the Michelson and unequal-arm Michelson TDI combinations.

arrival of the beams at spacecraft 1, we get

$$\begin{aligned} & [y_{3-21}(t) + y_{123,-2}(t)] - [y_{231}(t) + y_{1-32,3}(t)] \\ & - \frac{1}{2}(z_{231,-33}(t) - z_{3-21,2-2}(t)) + \frac{1}{2}(z_{231}(t) - z_{3-21}(t)), \end{aligned} \quad (11)$$

where the comma notation $y_{slr,d_1d_2\dots}$ denotes retardation by the armlengths L_{d_1} , L_{d_2} , and so on. Laser-noise cancellation works in this case because the length of the two

paths $1 \rightarrow 3 \rightarrow 1$ and $1 \rightarrow 2 \rightarrow 1$ is the same ($2L$), so we can line up both the starting and the ending points of the two paths. If the arms (and hence the paths) were unequal, we would be left with residual laser noise originating from the starting points of the two paths, as given by

$$- \left(\frac{1}{2}C_{1,-33}(t) - \frac{1}{2}C_{1,2-2}(t) \right) + \left(\frac{1}{2}C_{1,2-2}^*(t) - \frac{1}{2}C_{1,-33}^*(t) \right), \quad (12)$$

The case of unequal (but constant) arms is tackled successfully by using new paths ($1 \rightarrow 3 \rightarrow 1 \rightarrow 2 \rightarrow 1$ and $1 \rightarrow 2 \rightarrow 1 \rightarrow 3 \rightarrow 1$) each of which traces out *both* original paths ($1 \rightarrow 2 \rightarrow 1$ and $1 \rightarrow 3 \rightarrow 1$), but in opposite orders (see right panel of Fig. 5). In this case, if we set the two paths to end at time t , the times of departure are both $t - (L_2 + L_{-2}) - (L_{-3} + L_3)$, and the z_{slr} correction terms can cancel the noise emitted at that time, as well as time t . The corresponding TDI combination [known as unequal-arm-Michelson X , and first derived by Tinto & Armstrong (1999)] is

$$\begin{aligned} X = & [y_{1-32,32-2} + y_{231,2-2} + y_{123,-2} + y_{3-21}] - [y_{123,-2-33} + y_{3-21,-33} + y_{1-32,3} + y_{231}] \\ & - \frac{1}{2}(z_{3-21,2-2-33} - z_{231,-332-2}) - \frac{1}{2}(z_{3-21} - z_{231}) \\ & + \frac{1}{2}(z_{3-21,2-2} - z_{231,2-2}) + \frac{1}{2}(z_{3-21,-33} - z_{231,-33}) \end{aligned} \quad (13)$$

where we omitted the dependence on t common to all the terms.

Many TDI combinations are possible: all cancel laser noise, but each shows a different coupling to GWs and to the remaining system noises (known collectively as *secondary noises*). As the understanding of TDI improved, the standard TDI observables evolved through various generations, capable of canceling laser noise for increasingly complex LISA geometries:

First-generation TDI. Also known as TDI 1.0. The first-generation TDI observables (Tinto & Armstrong 1999; Armstrong et al. 1999; Estabrook et al. 2000; Armstrong et al. 2001) cancel laser noise exactly in LISA configurations with unequal (but constant) arms, and $L_k = L_{-k}$. Interferometric combinations of various types are possible:

The *Sagnac-type observables* (α , β , γ) are sums of six basic Doppler observables, and they involve the difference between the Doppler shifts accumulated by light propagating around the LISA array in the two senses. Thus, the Sagnac-type observables use all the LISA laser links in both directions. A fully symmetric Sagnac observable (ζ) is considerably less sensitive than most others to GWs with frequencies at the lower end of the LISA band; it was suggested (Tinto et al. 2000; Hogan & Bender 2001) that the comparison between the

power observed in ζ and in the other TDI variables could be used to discern a stochastic GW background from instrumental noise. The observables built from six Doppler variables are also known as *six-pulse combinations*, because their response to an impulsive plane GW consists of six separate pulses.

Eight-pulse combinations involve sums and differences of the Doppler shifts measured along four of the six LISA laser links. The *unequal-arm Michelson observables* (X , Y , Z) use both links of two arms; as discussed above, they can be interpreted as measuring the phase difference accumulated by light traveling (twice, in opposite orders) along the two arms of a Michelson interferometer centered in one of the spacecraft. Perhaps for this reason, and in analogy with ground-based GW interferometers, a single unequal-arm Michelson observable (generally X) is often used in LISA data analysis to compute expected detection rates and parameter-estimation accuracies.

More eight-pulse combinations can be formed: the *beacon* observables (P , Q , R) use only the two links departing from one of the spacecraft, and both links along the opposite arm; the *monitor* observables (E , F , G) use only the two links arriving at one of the spacecraft, and both links along the opposite arm; last, the *relay* observables (U , V , W) use one departing link and the adjacent arriving link at one of the spacecraft, together with both links along the opposite arm. The eight-pulse combina-

tions can be considered as LISA fail-safe modes, because they are available even if one or two of the laser links fail. Note however that all six lasers must still be available to build the intra-spacecraft observables z_{slr} required for the eight-pulse combinations, except in the case of the unequal-arm Michelson observables: one of these can always be built even if one or both lasers directed along one of the arms happen to fail.

Dhurandhar et al. (2002) proved that the space of all the first-generation TDI observables can be constructed by combining four generators, which they identify in α , β , γ , and ζ . Prince et al. (2002) showed how to diagonalize the cross noise spectrum of the generators to obtain three observables (A , E , and T) *with uncorrelated noises*. The three *optimal observables* A , E , and T are written as sums and differences of α , β , and γ , and when used in combination they achieve the optimal S/N for GW sources at any frequency in the LISA band.

Modified TDI. Also known as TDI 1.5. Shaddock (2004) recently pointed out that the rotation of the LISA array introduces a difference in the armlengths experienced by beams traveling in the corotating and counterrotating directions (i.e., $L_k \neq L_{-k}$). Furthermore, this difference becomes much larger if we take into account also the orbital motion of the array around the Sun (Tinto et al. 2004). Some of the first-generation observables (the X -type, P -type, E -type, and U -type combinations), cancel laser noise also for $L_k \neq L_{-k}$, if time delays for the appropriate oriented arms are used [as we have already arranged, for instance, in Eq. (14)]; these observables can be interpreted as tracing light paths that enclose vanishing areas. Conversely, the first-generation observables that trace light paths that enclose a finite area (such as α , β , γ , and ζ) are equivalent to *Sagnac interferometers* (Ashby 2003), and must necessarily be sensitive to the rotation of the array, which shows up as a spurious phase difference between the lasers, originating from the starting points of the light paths. The Sagnac observables can be modified by means of a finite-difference procedure analogous to the change undergone between the equal-arm and unequal-arm Michelson combinations (see Fig. 5), so that the modified Sagnac observables have null enclosed area, and cancel laser noise (Cornish & Hellings 2003; Shaddock et al. 2003). The resulting combinations [α_1 , α_2 , and α_3 , which generalize α , β , and γ ; and ζ_1 , ζ_2 , and ζ_3 (Tinto et al. 2004), which nonuniquely generalize ζ] include twice as many y_{slr} variables as the first-generation combinations (i.e., they are 12-pulse observables).

Second-generation TDI. Also known as TDI 2.0. The motion of the LISA array introduces not only a directional dependence of the armlengths, but also a time dependence, as first recognized by Cornish & Hellings (2003). In this case, the order of the TDI retardations becomes important: for instance, if the armlengths are constant, then

$$t_{;2-2} \equiv t - L_{-2} - L_2 = t - L_2 - L_{-2} \equiv t_{;-22} \quad (14)$$

but if they are not (as signaled by a semicolon index notation), then

$$\begin{aligned} t_{;2-2} &\equiv (t - L_{-2}(t) - L_2(t - L_{-2})) \\ &\neq (t - L_2(t) - L_{-2}(t - L_2)) \equiv t_{;-22}. \end{aligned} \quad (15)$$

More generally, the semicolon notation represents the retardation chain rule

$$\begin{aligned} t_{;d_1 \dots d_n} &= t - L_{d_n}(t) - L_{d_{n-1}}(t - L_{d_n}(t)) \\ &\quad - L_{d_{n-2}}(t - L_{d_n}(t) - L_{d_{n-1}}(t - L_{d_n}(t))) - \dots \end{aligned} \quad (16)$$

where the rightmost retardation index is applied first, using the armlength $L_{d_n}(t)$; the next-to-rightmost retardation index is applied second, using the partially retarded armlength $L_{d_{n-1}}(t - L_{d_n}(t))$, and so on. Taylor-expanding the armlengths, and retaining only the zeroth-order and first-order terms, we get

$$\begin{aligned} t_{;d_1 \dots d_n} &= t - L_{d_n} - \left[L_{d_{n-1}} - \dot{L}_{d_{n-1}} L_{d_n} \right] \\ &\quad - \left[L_{d_{n-2}} - \dot{L}_{d_{n-2}} (L_{d_n} + L_{d_{n-1}}) \right] - \dots \end{aligned} \quad (17)$$

where for ease of notation we have dropped the (t) dependence common to all the armlengths. As discussed by Cornish & Hellings (2003), Shaddock et al. (2003), and Tinto et al. (2004), the eight-pulse TDI observables can be generalized, once again by a procedure akin to finite differentiation, to 16-pulse observables that cancel laser noise up to first order in the Taylor-expanded armlengths; for the LISA orbital parameters, this is more than enough to cancel laser noise to a level below the secondary noises. According to the notation of Tinto et al. (2004), X_1 , X_2 , and X_3 generalize X , Y , and Z ; P_1 , P_2 , and P_3 generalize P , Q , and R ; E_1 , E_2 , and E_3 generalize E , F , and G ; and U_1 , U_2 , and U_3 generalize U , V , and W . The X_k observables can be interpreted as expressing the difference in laser phase between beams propagating along two paths whose Taylor-expanded total lengths differ only by terms proportional to \ddot{L}_k or to higher derivatives;⁵ the residual laser noise is then a sum of expressions similar to

$$\begin{aligned} C_{k;A}(t) - C_{k;B}(t) &\simeq \dot{C}_k(t) \times [t_{;A} - t_{;B}] \\ &\simeq \dot{C}_k(t) \times O[\ddot{L} \text{ and higher derivatives}]. \end{aligned} \quad (18)$$

As for the Sagnac-type observables, the 12-pulse modified observables α_1 , α_2 , α_3 , ζ_1 , ζ_2 , and ζ_3 can already cancel laser noise to a level below the LISA secondary noises: the residual laser noise is of order \dot{L} and higher, but the specific combination of \dot{L}_k involved turns out to be small for the LISA orbit.

Although historically the TDI observables were derived by combining time-shifted combinations of the basic (one-way) Doppler measurements $y_{slr}(t)$, they can also be written as combinations of one-way and two-way Doppler measurements, generated by locking five of the six lasers to the remaining one, as described by Tinto et al. (2003); the resulting expressions contain fewer terms, are still noise-canceling, and have the same response to GWs.

3. IMPLEMENTATION AND USAGE OF *SYNTHETIC LISA*

Synthetic LISA is an object-oriented C++ library built to mirror the idealized structure shown in Fig. 1. Each

⁵ The finite differencing procedure adopts the compound paths $A \equiv I+II$ and $B \equiv II+I$, where the paths I and II must contain the same links, in different orders; then $t_{I,II} - t_{II,I} \simeq \dot{I} \times II - \dot{II} \times I \equiv (\sum_i \dot{L}_{I_i})(\sum_j L_{II_j}) - (\sum_i \dot{L}_{II_i})(\sum_j L_{I_i}) = 0$.

block in the figure corresponds to one or more C++ classes [i.e., smart structures that may contain data and customized methods to be applied on the data (Stroustrup 2000)]. A typical *Synthetic LISA* session follows this object-oriented structure. For instance:

1. Create an instance of a LISA geometry class (`LISA`) with the desired orbital parameters.
2. Create instances of a LISA noise class (`Noise`) for the 18 fundamental-noise time series defined in Sec. 2.3, tuning noise parameters if so desired. (This step is optional, since the class `TDInoise` can create its own standard noise objects.)
3. Create an instance of a GW source class (`Wave`) of the desired type and parameters.
4. Create an instance of a LISA TDI class (`TDInoise` or `TDIsignal`), feeding it the LISA geometry, LISA noises, and GW source objects previously created.
5. Use the TDI object (by calling one of its methods) to generate a time series of the TDI observables and write it to disk or memory.

No C++ programming and compilation is needed to use *Synthetic LISA*, because the functionality of the package can be accessed very easily from the scripting language Python,⁶ either interactively, or with short scripts: the *Synthetic LISA* session described above would translate to a handful of lines in Python. *Synthetic LISA*'s object-oriented implementation is especially useful for targeted investigations that compare multiple configurations of one object (for instance, one of the fundamental noises, or the GW source), while all other objects are kept fixed.

In the rest of this section, we describe the implementation of all the *Synthetic LISA* objects. In Sec. 3.1, we give common notations and conventions; in Sec. 3.2, we discuss the LISA geometry objects; in Sec. 3.3, we turn to GW source objects, and their use in the `TDIsignal` class; in Sec. 3.4, we describe LISA noise objects, and their use in the `TDInoise` class. Note that the implementation of TDI in *Synthetic LISA* is not based on fixed-timestep sequences, but rather on methods that can return the noises and GW signals at arbitrary nonquantized times, as needed by the TDI observables. However, some objects (such as pseudorandom or sampled noise sequences) are maintained internally by *Synthetic LISA* as arrays, and then interpolated to the TDI delayed times: see Sec. 4.2 for a discussion of the interpolation and bandlimitedness of pseudorandom noises and of presampled noises and GW signals. The syntax of *Synthetic LISA*'s commands is described in detail in the Appendix.

3.1. Conventions

Our convention, introduced in Sec. 2 and shown in Fig. 3, is to label the three LISA spacecraft as 1, 2, 3, and to label the (oriented) LISA arm l corresponding to transmission from spacecraft s to r as $l = \{1, 2, 3\}$ for $(s, r) = \{(3, 2), (1, 3), (2, 1)\}$, and $l = \{-1, -2, -3\}$ for $(s, r) = \{(2, 3), (3, 1), (1, 2)\}$ (thus, $\text{sgn}(l) = \epsilon_{s||r}$). The motion of the LISA *guiding center* (the baricenter of the

array) is approximately contained in the plane of the ecliptic; for this and other reasons (Tinto et al. 2004), it is convenient to work in a Solar-system–baricentric ecliptic coordinate system (for short, SSB frame); we take the x axis of this system to be directed toward the vernal point. Throughout *Synthetic LISA*, we take $G = c = 1$, and $1 \text{ yr} = 31,536,000 \text{ s}$.⁷

3.2. LISA geometry

There are different levels of complexity at which the motion of the LISA array, discussed in Sec. 2.1, can be modeled in a simulation of the LISA science process; correspondingly, increasingly sophisticated TDI observables are needed to cancel laser noise once the added complexity is taken into account. In *Synthetic LISA*, these levels correspond to different derived classes of the base class `LISA` (in C++, a derived class inherits the data content and behavior of its base class, and can add enhancements or customizations); users can choose the `LISA` class that best fits their needs.

All the `LISA` classes define the methods `putp`, `putn`, and `armlength`, which return $\vec{p}_i(t)$, $\hat{n}_i(t)$, and $L_i(t)$ (see Table A2 for their syntax). The armlengths and photon-propagation vectors computed by these functions account for the aberration effects caused by the finite speed of light and by the spacecraft motion intervening between the events of pulse emission and reception, as specified in Sec. 2.2.

The derived `LISA` classes currently defined in *Synthetic LISA* are the following; the syntax of the corresponding constructors is given in Table A2.

OriginalLISA. At the simplest level, we ignore the LISA motion altogether, and put the spacecraft in a stationary triangular configuration in the plane of the ecliptic; this model was used implicitly in the development of first-generation TDI. The class `OriginalLISA` implements such a stationary configuration, with spacecraft positions \vec{p}_i set up according to the following rules:

1. the three armlengths are set to arbitrary values L_1 , L_2 , and L_3 ;
2. $\vec{p}_1 + \vec{p}_2 + \vec{p}_3 = 0$, so the baricenter of the constellation lies in the origin of the SSB ecliptic coordinate system;
3. $p_1^z = p_2^z = p_3^z = 0$, so the constellation lies in the $z = 0$ plane;
4. looking from above (from positive z 's), the spacecraft sequence $1 \rightarrow 2 \rightarrow 3 \rightarrow 1$ traces a clockwise path (x toward $-y$), while the arms labeled by positive indices trace a counterclockwise path (x toward y);
5. $p_1^y = 0$, so spacecraft 1 lies along the x axis.

ModifiedLISA. At the next level of complexity, we model the cartwheeling motion of the LISA array, but not its orbital motion around the Sun. To this purpose, we place the spacecraft in the plane of the ecliptic, and

⁷ This default can be altered by modifying the constants `secondsperyear` and `yearspersecond` in the header file `lisasim-lisa.h`.

⁶ Python website: www.python.org.

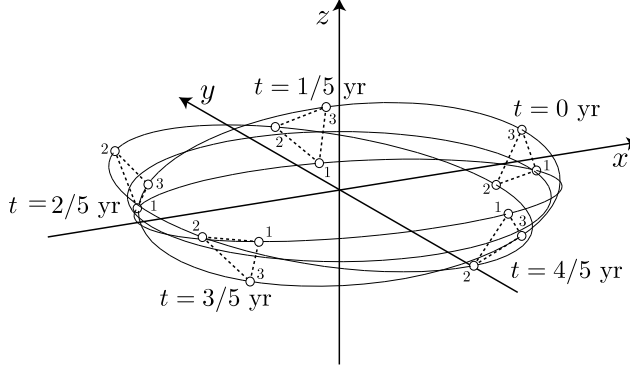


FIG. 6.— Orbital motion of the LISA detector, shown in a Solar-system-baricentric ecliptic coordinate system. The trajectories shown correspond to setting $\zeta = -\pi/6$, $\Omega = 2\pi/\text{yr}$, and $\xi_0 = \eta_0 = 0$. For this choice, at time $t = 0$ the LISA guiding center lies on the positive x axis of the SSB system, while \vec{p}_1 lies on the negative y axis. Figure excerpted from Królak et al. (2004).

we put them in rotation around their baricenter (which coincides with the origin of the SSB ecliptic coordinate system) with the angular frequency $\Omega = 2\pi/\text{yr}$. The class `ModifiedLISA` implements such a rotating configuration.

At the time $t = 0$, the positions of the three spacecraft coincide with their stationary `OriginallISA` positions; at subsequent times, they are computed by rotating the initial configuration counterclockwise (x toward y) through the angle Ωt . This model introduces a distinction between the armlengths experienced by light propagating along or against rotation (an example of the Sagnac effect (Ashby 2003)). Modified or second-generation TDI observables are then needed to cancel laser and optical-bench noise. Elementary kinematics shows that the corotating and counterrotating

⁸ According to the standard formula for the Sagnac effect (Ashby 2003), the difference in travel times for corotating and counterrotating paths enclosing the area A should be $4\Omega A/c^2$; in our case,

armlengths are given by

$$L_{\text{arm}} = L_{\text{arm}}^{\text{stat}} + \vec{\Omega} \cdot (\vec{p}_r \times \vec{p}_s) + O(\Omega^2), \quad (19)$$

for light propagating from spacecraft s to r , where $\vec{\Omega} = \Omega \hat{z}$, and $L_{\text{arm}}^{\text{stat}} = |\vec{p}_r - \vec{p}_s|$ is evaluated for stationary spacecraft positions (i.e., without rotation). With equal armlengths, the correction reduces⁸ to $\pm\Omega|L_{\text{arm}}^{\text{stat}}|^2/(2\sqrt{3})$, or about 1.6×10^{-5} s for the standard LISA armlength.

CircularRotating. At the next level of complexity, we include all the qualitative features of the LISA motion using the simplest possible geometry where the armlengths are constant (before aberration is taken into account). That is, we move the baricenter of the LISA array on a circular orbit in the ecliptic plane, while the array itself, inclined with respect to the ecliptic, rotates around the guiding center with the angular frequency Ω . The class `CircularRotating` implements such a rotating configuration.

This model was used by Królak et al. (2004) to derive analytic expressions of the LISA GW responses. Following the conventions of Królak et al. (2004), in the coordinate frame where the spacecraft are at rest, we set without loss of generality $\vec{p}_i^L = (L/\sqrt{3})(-\cos 2\sigma_i, \sin 2\sigma_i, 0)$, and $\hat{n}_i^L = (\cos \sigma_i, \sin \sigma_i, 0)$, where $\sigma_i = 3\pi/2 - 2(i-1)\pi/3$. A realistic set of spacecraft orbits, shown in Fig. 6, is then obtained by letting $\vec{p}_i(t) = \vec{r}(t) + O_2 \cdot \vec{p}_i^L$, where \vec{r} is the vector from the origin of the SSB coordinate system to the LISA guiding center, as described by the SSB components $\vec{r} = R(\cos \eta, \sin \eta, 0)$; here $R = 1 \text{ AU} = 499.004 \text{ s}$ and $\eta = \Omega t + \eta_0$ is the true anomaly of the LISA guiding center in its orbit around the Sun. The rotation matrix O_2 models the cartwheeling motions of the spacecraft along their inclined orbits, shown in Fig. 7; it is given by

we get a travel-time difference $\sqrt{3}|L_{\text{arm}}^{\text{stat}}|^2$, consistent with area of the LISA equilateral-triangle configuration.

$$O_2 = \begin{pmatrix} \sin \eta \cos \xi - \cos \eta \sin \xi \sin \xi & -\sin \eta \sin \xi - \cos \eta \sin \xi \cos \xi & -\cos \eta \cos \xi \\ -\cos \eta \cos \xi - \sin \eta \sin \xi \sin \xi & \cos \eta \sin \xi - \sin \eta \sin \xi \cos \xi & -\sin \eta \cos \xi \\ \cos \xi \sin \xi & \cos \xi \cos \xi & -\sin \xi \end{pmatrix}; \quad (20)$$

here $\xi = -\Omega t + \xi_0$ is the phase of the motion of each spacecraft around the guiding center, while ζ sets the inclination of the orbital plane with respect to the ecliptic. For the LISA trajectory, $\zeta = -\pi/6$ (LISA Study Team 1998). These spacecraft orbits can be mapped approximately to those used in the LISA Simulator (Cornish & Rubbo 2003) by setting $\eta_0 = \kappa$, $\xi_0 = 3\pi/2 - \kappa + \lambda$, where κ and λ are the parameters defined below Eqs. (56) and (57) of Cornish & Rubbo (2003), and by choosing $sw < 0$ in the `CircularRotating` constructor (Table A2), which has the effect of exchanging spacecraft 2 and 3.

The armlengths experienced by light propagating between the spacecraft can be found by solving Eq. (3) numerically. However, for reasons of efficiency, *Synthetic*

LISA employs the lowest-order approximation to the solution,

$$L_{\text{arm}} = L + (\text{sgn } \text{arm}) \times (\Omega R L) \sin(\Omega t - \delta_{\text{arm}}), \quad (21)$$

where $\delta_i \equiv \{\xi_0, \xi_0 + 4\pi/3, \xi_0 + 2\pi/3\}$. For the standard LISA orbits and configuration, the amplitude of this oscillating correction is about 1.6×10^{-3} , or 100 times larger than the correction due to the Sagnac effect alone for `ModifiedLISA`.

EccentricInclined. The most accurate description of the LISA motion available in *Synthetic LISA* models the eccentric orbits of the spacecraft up to second order in the eccentricity e . For these orbits, implemented by the class `EccentricInclined`, the dominant (and evolving) differences between the armlengths are caused by the flexing

motion of the array (Cornish & Hellings 2003) due to orbital eccentricities. Following Cornish & Rubbo (2003),

we set

$$\begin{bmatrix} p_i^x \\ p_i^y \\ p_i^z \end{bmatrix} = (1 \text{ AU}) \begin{bmatrix} \cos \alpha + e[\sin \alpha \cos \alpha \sin \beta_i - (1 + \sin^2 \alpha) \cos \beta_i] + O(e^2) \\ \sin \alpha + e[\sin \alpha \cos \alpha \cos \beta_i - (1 + \cos^2 \alpha) \sin \beta_i] + O(e^2) \\ -\sqrt{3}e \cos(\alpha - \beta) + O(e^2) \end{bmatrix}, \quad (22)$$

$$\alpha = \Omega t + \eta_0, \quad \beta_i = \eta_0 + \xi_0 - \sigma_i, \quad (23)$$

where $\sigma_i = 3\pi/2 - 2(i-1)\pi/3$ and $e = 0.00964838$, yielding an effective $L \simeq 16.6782$ s. The parameters η_0 and ξ_0 have approximately the same meaning as in `CircularRotating`. The correspondence to the LISA Simulator orbital parameters is again $\eta_0 = \kappa$, and $\xi_0 = 3\pi/2 - \kappa + \lambda$ (with $sw < 1$).

The armlengths experienced by light propagating along the arms can be found by solving Eq. (3). For efficiency, *Synthetic LISA* employs the lowest-order approximation

$$L_{\text{arm}} = L + \frac{1}{32}(eL) \sin(3\Omega t - 3\xi_0) + \left[(\text{sgn arm})(\Omega RL) - \frac{15}{32}(eL) \right] \sin(\Omega t - \delta_{|\text{arm}|}), \quad (24)$$

where $\delta_i \equiv \{\xi_0, \xi_0 + 4\pi/3, \xi_0 + 2\pi/3\}$. The amplitude of the flexing correction is about 7.5×10^{-2} s, or 0.5% of the nominal LISA armlength; the rate of change of the armlengths is about 1.5×10^{-8} s/s, which requires second-generation TDI to yield sufficient cancellation of laser phase noise.

3.3. The `Wave` class and the LISA GW response

In *Synthetic LISA*, the GW response of the TDI observables is obtained from the class `TDISignal`, which inherits from the base class `TDI` the definitions of the observables in terms of the basic Doppler responses, but

⁹ The `TDISignal` method `z` for z_{slr} always returns zero, since the GW response of the intraspacecraft Doppler observable z_{slr} is

which also defines the method `y` for y_{slr} , according to Eq. (1).⁹ A `TDISignal` object is created (see Table A5) by specifying a LISA geometry object (Sec. 3.2) and a GW source object; the latter is always derived from the base class `Wave`.

All `Wave` classes share the same geometrical setup, which follows the conventions of Królak et al. (2004). At the position \vec{x} in the SSB frame, the spatial part of the transverse-traceless metric perturbation associated with a plane GW can be written as

$$h(t) = h_+(t - \hat{k} \cdot \vec{x}) \mathbf{e}_+ + h_\times(t - \hat{k} \cdot \vec{x}) \mathbf{e}_\times; \quad (25)$$

here the functions $h_+(t)$ and $h_\times(t)$ express the two polarization components of the wave at time t , measured at the origin of the SSB frame. For a GW source at ecliptic latitude β and ecliptic longitude λ , the unit propagation vector \hat{k} is

$$\hat{k} \equiv -(\cos \beta \cos \lambda, \cos \beta \sin \lambda, \sin \beta). \quad (26)$$

The two polarization tensors \mathbf{e}_+ and \mathbf{e}_\times that appear in Eq. (25) can be defined without loss of generality as

$$\mathbf{e}_+ \equiv \mathbf{E} \cdot \begin{pmatrix} 1 & 0 & 0 \\ 0 & -1 & 0 \\ 0 & 0 & 0 \end{pmatrix} \cdot \mathbf{E}^T, \quad \mathbf{e}_\times \equiv \mathbf{E} \cdot \begin{pmatrix} 0 & 1 & 0 \\ 1 & 0 & 0 \\ 0 & 0 & 0 \end{pmatrix} \cdot \mathbf{E}^T, \quad (27)$$

where the orthogonal matrix \mathbf{E} ,

null, at least if the lasers are not phase-locked to a master.

$$\mathbf{E} \equiv \begin{pmatrix} \sin \lambda \cos \psi - \cos \lambda \sin \beta \sin \psi & -\sin \lambda \sin \psi - \cos \lambda \sin \beta \cos \psi & -\cos \lambda \cos \beta \\ -\cos \lambda \cos \psi - \sin \lambda \sin \beta \sin \psi & \cos \lambda \sin \psi - \sin \lambda \sin \beta \cos \psi & -\sin \lambda \cos \beta \\ \cos \beta \sin \psi & \cos \beta \cos \psi & -\sin \beta \end{pmatrix}, \quad (28)$$

expresses an Euler rotation sequence, whereby the β and λ terms can be understood as enforcing the transversality of the GW, while the polarization angle ψ encodes a rotation around the direction of wave propagation, $-\hat{k}$, setting the convention used to define the two polarizations. The polarizations corresponding to $\psi = 0$ are shown in Fig. 8 for various source positions in the sky. The positional parameters β , λ , and ψ can be mapped to the parameters θ , ϕ , and ψ used in the LISA Simulator (Cornish & Rubbo 2003) by setting $\beta = \pi/2 - \theta$, $\lambda = \phi$, and $\psi = -\psi$.

All the `Wave` classes define the methods `hp(t)` and `hc(t)`, which return $h_+(t)$ and $h_\times(t)$. The derived `Wave` classes currently defined in *Synthetic LISA* are the following; the syntax of the corresponding constructors is given in Table A3.

SimpleBinary. The class `SimpleBinary` implements a simple monochromatic binary, wherein

$$\begin{bmatrix} h_+(t) \\ h_\times(t) \end{bmatrix} = A \begin{bmatrix} (1 + \cos^2 \iota) \times \cos(2\pi ft + \phi_0) \\ (2 \cos \iota) \times \sin(2\pi ft + \phi_0) \end{bmatrix}, \quad (29)$$

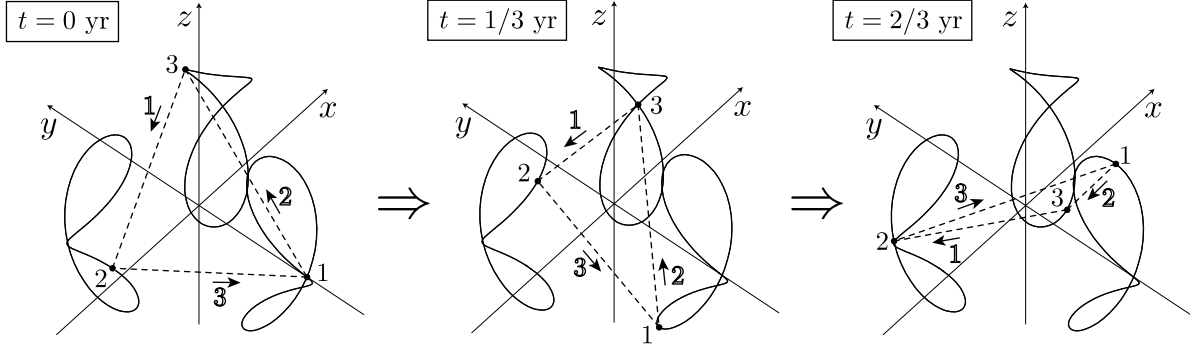


FIG. 7.— Cartwheeling motion of the LISA array, as plotted in a frame with center in the LISA guiding center and axes parallel to the SSB ecliptic frame. We show three snapshots at different times along the LISA orbital period, 1 yr. Figure excerpted from Królak et al. (2004).

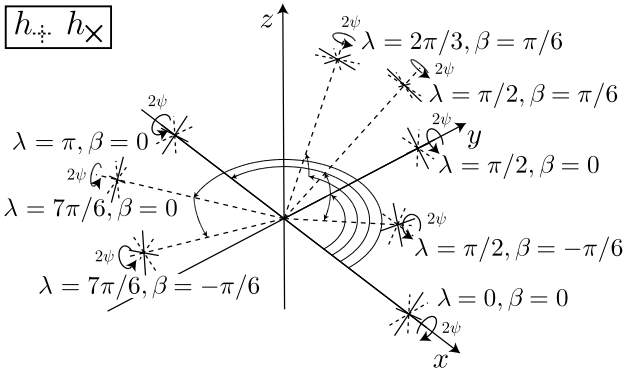


FIG. 8.— Conventional definition of the GW polarizations + (dashed) and \times (solid) for various ecliptic latitudes β and longitudes λ . Figure excerpted from Królak et al. (2004).

where A is the common amplitude,¹⁰ ι is the inclination angle, f is the GW frequency observed in the SSB frame, and ϕ_0 is the phase at $t = 0$.

InterpolateMemory. The class `InterpolateMemory` allows users to provide their own $h_+(t)$ and $h_\times(t)$ functions, given as arrays of floating-point numbers equispaced in time. Linear interpolation is used to compute h_+ and h_\times at intermediate times, as requested by the user or as needed by the TDI process.

User-defined Wave classes. If more flexibility or precision is needed than allowed by `InterpolateMemory`, users can add their own C++ derived `Wave` classes, which can implement any functional dependence for $h_+(t)$ and $h_\times(t)$ (see Table A3).

3.4. The `Noise` class and the LISA noise response

In *Synthetic LISA*, the response of the TDI observables to the fundamental LISA noises is obtained from the class `TDInoise`, which inherits from the base class `TDI` the definitions of the observables in terms of the basic Doppler responses, but which also defines the methods `y` and `z` for

¹⁰ The standard value of A is $(2m_1m_2/dR)$ with m_1, m_2 the two masses, d the luminosity distance, and R the orbital separation. The common amplitude h_0 used by Królak et al. (2004) differs by a factor of two ($h_0 = 2A$), absorbed in h_\times^0 and h_+^0 .

y_{slr} and z_{slr} according to Eqs. (8) and (9). A `TDInoise` object is created by specifying a LISA geometry object (Sec. 3.2) and a prescription for the 18 fundamental noise variables discussed in Sec. 2.3. In *Synthetic LISA*, fundamental noises are represented by derived classes of the base class `Noise`.

All the `Noise` objects available in *Synthetic LISA* are based on the following three-stage model, implemented in `InterpolateNoise`; the syntax of the corresponding constructors is given in Table A4.

1. *Generation.* In the first stage, a sequence of noise samples with user-defined sampling timestep Δt is obtained as a user-provided array (e.g., from experimental measurements), or by means of a pseudorandom number generator. *This noise is always understood to be bandlimited at the Nyquist frequency $f_c = (2\Delta t)^{-1}$; thus, it is completely specified (at any time between the samples) by the sequence of samples.* *Synthetic LISA* employs Luescher's lagged Fibonacci generator (Luescher 1994), as implemented in the *GNU Scientific Library*,¹¹ to generate independent, uniformly distributed deviates; the uniform deviates are then converted into Gaussian deviates by means of the Box–Muller transform (Box & Muller 1958). The result is white Gaussian noise with zero mean and unit variance.

2. *Filtering.* In the second stage, the noise sequences are filtered, if so desired, through simple digital time-domain filters to reshape their power spectra. The current version of *Synthetic LISA* provides the finite-difference filter $y[n\Delta t] = x[n\Delta t] - x[(n-1)\Delta t]$ (with x the original noise sequence), which has the power transfer function $|1 - \exp(2\pi if\Delta t)|^2 = 4\sin^2(\pi f\Delta t)$, and the damped-integrator filter $y[n\Delta t] = \alpha y[(n-1)\Delta t] + x[n\Delta t]$, which has power transfer function $(1/4)\sin^{-2}(\pi f\Delta t)$ in the limit $\alpha \rightarrow 1$ (the damping, set by default to $\alpha = 0.9999$, is needed to control the DC component of the integrated noise).

In *Synthetic LISA*, pseudorandom white noise fil-

¹¹ GNU Scientific Library, v. 1.4 (2003): www.gnu.org/software/gsl.

tered through the finite-difference and damped-integrator filters is used to approximate the standard optical-path and proof-mass noises defined in Sec. 2.3, which have spectral densities proportional to $f^{\pm 2}$ (rather than $[4 \sin^2(\pi f \Delta t)]^{\pm 1}$). The approximation is good if f_c is chosen sufficiently higher than the highest frequency at which one wishes to analyze the TDI noise responses (but of course lower than the Nyquist frequency used to sample the TDI observables, to avoid aliasing).

3. Interpolation. In the third stage, the samples are normalized and interpolated to provide the properly dimensioned value of the noise process at arbitrary times (not necessarily multiples of Δt), as required by the TDI observables. Linear and higher-order Lagrange interpolation schemes are available in *Synthetic LISA*. The frequency response of the interpolation procedure is crucial to the simulation and is discussed in detail in Sec. 4.2. The basic fact is that interpolation spreads the power of the bandlimited sampled noise to frequencies higher than f_c ; some of this power will alias back into the spectrum of the TDI observables, because these are built in the time domain with exact time delays, and thus they can pick up the spurious high-frequency noise components. It is then essential to control the frequency response of interpolation, and to choose the sampling timestep, for both the fundamental noises and TDI, as needed to reduce aliasing.

3.5. LISA TDI observables

By way of the base class TDI, the `TDISignal` and `TDInoise` classes define the methods `obs(t)`, which return the value of the TDI observables (first generation, modified, and second generation) listed in Tab. A5. The user can define additional observables by adding new definitions to the TDI class (in C), or by using explicit combinations of the `y` and `z` methods (in Python).

4. TESTS AND APPLICATIONS OF *SYNTHETIC LISA*

In this section we present examples of tests and applications for *Synthetic LISA*, ranging from elementary checks (on the spectral densities of the fundamental noises, in Secs. 4.1 and 4.2; on the noise spectra of the TDI observables, in Sec. 4.3; on monochromatic GW signals, in Sec. 4.5) to numerical simulations dealing with important implementation issues (on the imperfect cancellation of laser phase noise with first-generation TDI and with noisy armlength measurements, in Sec. 4.4). The *Synthetic LISA* distribution includes all the scripts that were used to run these tests and simulations. Except where otherwise specified, for all the power spectra displayed in this section we reduced spectral leakage and fluctuations by dividing the time series into partially overlapping segments (in number of 64 to 1024, depending on the specific test), triangle-windowing each segment, and averaging the resulting power spectra, as described by Press et al. (1992).

4.1. Standard LISA noises

As a first check on the implementation of *Synthetic LISA*, we use the `InterpolateNoise` class to generate

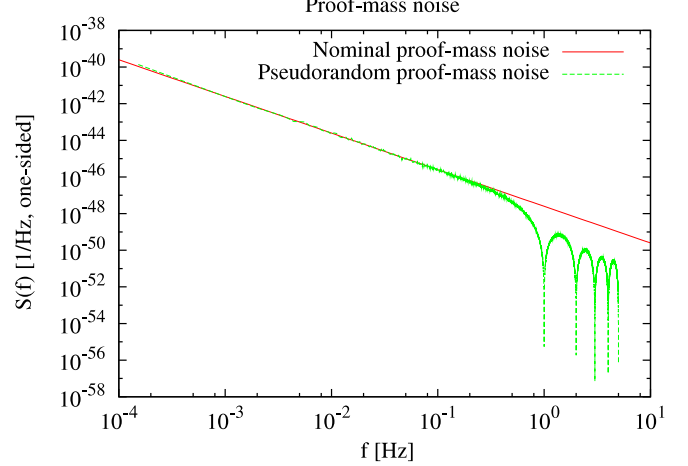


FIG. 9.— Pseudorandom proof-mass noise generated by `InterpolateNoise(1.0, 256.0, 2.5e-48, -2.0, 1)` (dashed), and ideal proof-mass-noise spectral density (solid). The spectrum was produced by the *Synthetic LISA* example script `test-proofnoise`.

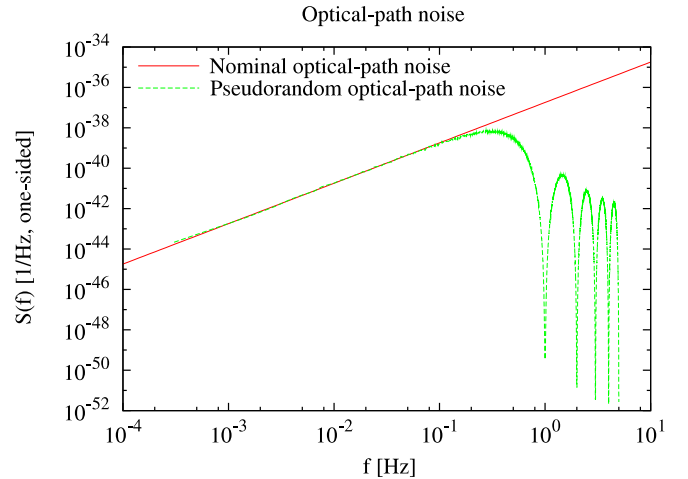


FIG. 10.— Pseudorandom optical-path noise generated by `InterpolateNoise(1.0, 256.0, 1.8e-37, 2.0, 1)` (dashed), and ideal optical-path-noise spectral density $S_n^{\text{OP}} = 1.8 \times 10^{-37} [\text{f/Hz}]^2 \text{ Hz}^{-1}$ (solid). The spectrum was produced by the *Synthetic LISA* example script `test-optnoise`.

pseudorandom series of the LISA fundamental noises with the standard spectral densities described in Sec. 2.3, and we compute their spectra. Figures 9–11 show our results for proof-mass noise, optical-path noise, and laser frequency noise respectively. For these tests, we generated pseudorandom noise with a timestep of 1 s (and therefore an ideal bandlimit frequency $f_b = 0.5$ Hz), and we resampled the process to a timestep of 0.1 s (and therefore a Nyquist frequency $f_N = 5$ Hz) using linear interpolation.

We see that the power spectra of the pseudorandom time series (dashed) adhere rather faithfully to the theoretical curves (solid), except at frequencies comparable to f_b , where the effect of interpolation is that noise power is not cut off sharply, but rather drops off smoothly (if

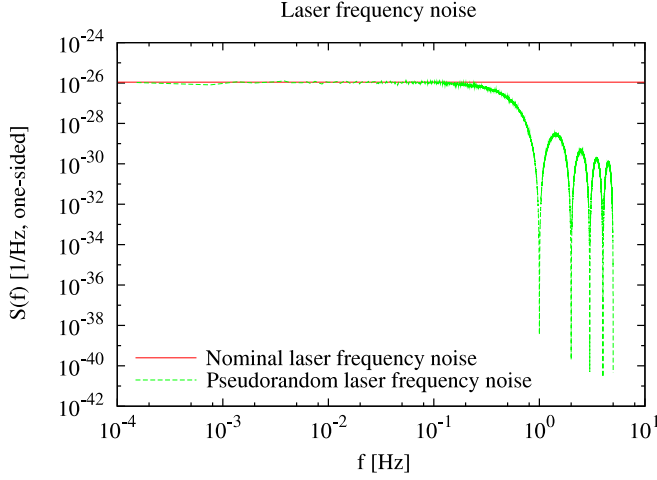


FIG. 11.— Pseudorandom laser frequency noise generated by `InterpolateNoise(1.0, 256.0, 0.1, 1.1e-26, 0.0, 1)` (dashed), and ideal laser-frequency-noise spectral density $S_n^{ls} = 1.1 \times 10^{-26} \text{ Hz}^{-1}$ (solid). The spectrum was produced by the *Synthetic LISA* example script `test-lasernoise`.

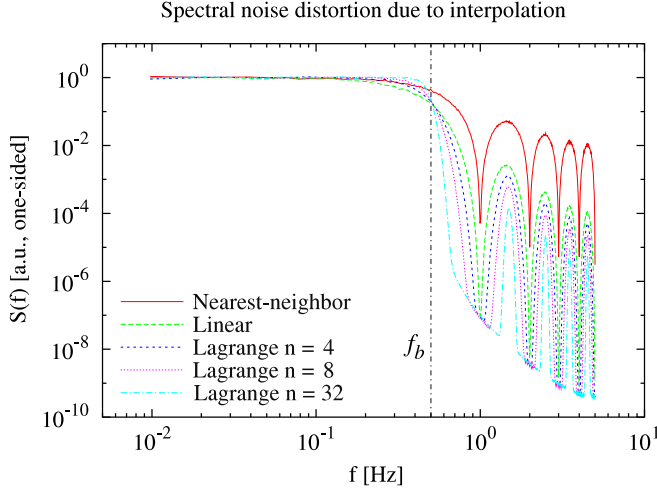


FIG. 12.— Noise distortion for 0.5 Hz-bandlimited white noise, with different interpolation schemes. Higher-order interpolation corresponds to a sharper transition at the bandlimit frequency and to lower ripples and deeper valleys between them (in this graph, the valleys are cut off by spectral leakage from the main platform at power = 1). The spectra were produced by the *Synthetic LISA* example script `test-interpolation`.

rapidly), with nulls at the harmonics¹² of f_b ; interpolation is discussed further in the next section. For the optical-path and proof-mass noises, the effect of interpolation is compounded by the effect of the finite-difference and finite-integration time-domain filters, whose transfer function is proportional to $\sin^{\pm 2}[\pi f/(2f_b)]$.

4.2. Frequency response of noise interpolation

In *Synthetic LISA*, pseudorandom noise is created by generating a sequence of uncorrelated Gaussian deviates,

¹² It is interesting to notice that for the f^2 optical-path noise (Fig. 10) the locations of the nulls conspire to reduce the aliasing of power to low frequencies, where the nominal f^2 power is lower than the envelope of interpolation-error power above f_b .

which are then interpreted as the sampled values at times $t_n = n\Delta t$, for $n = 0, 1, \dots$ of a continuous random noise process. The process is assumed to be bandlimited below¹³ $f_b = 1/(2\Delta t)$: by the sampling theorem (see, e.g., Press et al. 1992), the noise process can then be reconstructed perfectly at any intervening time t by convolving the sampled sequence with the interpolating kernel

$$\text{sinc}[\pi(t - t_n)/\Delta t] = \frac{\sin[\pi(t - t_n)/\Delta t]}{[\pi(t - t_n)/\Delta t]}. \quad (30)$$

Since the sinc kernel has infinite extent, it is of limited utility; however, a vast class of practical interpolation schemes, including the linear and Lagrange interpolators implemented in *Synthetic LISA*, can be formulated as the convolution of the sampled sequence with an interpolating kernel that is in some sense an approximation to a sinc.

The tradeoff in the approximation is between the number of samples used to interpolate and the sharpness of the spectral response. The correct sampling of a bandlimited process preserves all the spectral information below the Nyquist frequency, but it populates Fourier space with infinitely many exact replicas of the original spectrum, centered at frequencies $k/\Delta t$, for $k = \pm 1, \pm 2, \dots$. The effect of sinc interpolation is to multiply this composite spectrum by the Fourier transform of the sinc, which is a perfect square window of height 1 and width $1/\Delta t$, centered at $f = 0$. Thus, sinc interpolation achieves perfect signal reconstruction by selecting only the original spectrum and deleting all unwanted replicas. Practical schemes with kernels of finite extent cannot have such sharp frequency response, so they distort (amplify or suppress, depending on frequency) the original spectral content in the passband below f_b , and they allow some of the power of the unwanted spectral replicas to creep back into the interpolated process (either directly, if the process is sampled with a sufficiently high Nyquist frequency, or by aliasing to frequencies in the passband).

These effects can be observed in Fig. 12, which shows the spectrum of pseudorandom white noise, generated with a timestep of 1 s, and resampled to a timestep of 0.1 s, using no interpolation (i.e., defaulting to the nearest 1-s sample), linear interpolation, and Lagrange-polynomial interpolation of order 4, 8, and 32. In all cases, power begins to drop before the nominal bandlimit frequency of 0.5 Hz, but the drop is sharper for higher-order interpolation methods. Spurious power above the bandlimit frequency appears as *ripples* between the f_b harmonics: the height of the ripples decreases with interpolation order, while the valleys among them become wider. In Fig. 12, the valleys appear to be cut off by a common downgrading envelope; this is an artifact of spectral estimation due to the residual leakage from the platform below the passband; spectral leakage also smears out the nulls at the f_b harmonics to a finite height.

We conclude that the pseudorandom noise sequences generated by *Synthetic LISA* can be accurate representations of the idealized LISA noises defined in Sec. 2.3,

¹³ The application of time-domain filters does not change this picture: since the filters are linear, they do remodel the initially white spectrum, but the resulting time series can still be interpreted as the sampled version of a bandlimited continuous process.

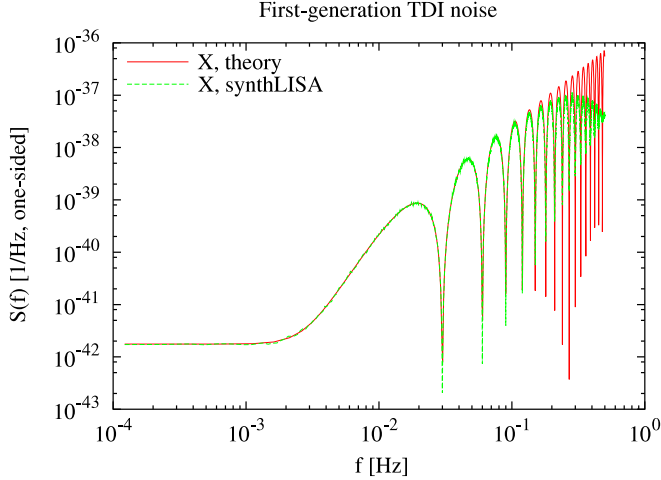


FIG. 13.—Spectral density of the first-generation TDI observable X for a stationary, equal-arm interferometer with $L_i = 16.6782$ s (solid curve), as compared with the analytical expression (4.1) of Estabrook et al. (2000) (dashed). At the high-frequency end of the plot, the *Synthetic LISA* curve is suppressed by the effects of linear noise interpolation and of the finite-difference time-domain filter; the envelope traced out by the nulls is an artifact of spectral leakage and of the number of points used to draw the theoretical curve. These spectra were produced by the *Synthetic LISA* example script `test-tdiequal-X`.

and therefore can be used to study the noise response of the TDI observables, as long as we take into account the effect of interpolation at frequencies comparable to f_b . Using linear interpolation (the default), it is probably safe to draw conclusions for frequencies $\lesssim f_b/5$; using higher-order interpolation it becomes possible to push our inferences to higher frequencies (however, when using our pseudorandom secondary noises, one should also be mindful of the fact that their spectral shape near f_b is $\sin^{\pm 2} \pi f/(2f_b)$ rather than $f^{\pm 2}$). The arguments made in this section apply also to the interpolated noise obtained from user-provided sampled-noise sequences, as long as the sampled noise can be considered bandlimited below its nominal Nyquist frequency.

See Shaddock et al. (2004) for a discussion of the use of interpolation in reconstructing the TDI observables on Earth from the y_{slr} and z_{slr} data, sampled onboard at a limited rate that can be transmitted affordably to Earth.

4.3. Secondary noises in the TDI observables

We now move on to full-fledged TDI, and we examine the spectra of the first-generation TDI observables for a stationary LISA configuration (**OriginalLISA**), with the purpose of verifying our results against analytical expectations, and of providing an explicit demonstration of laser-noise cancellation.

Figure 13 shows the spectrum of X in the case of equal, nominal arms ($L = 16.6782$ s); the solid line plots the analytical expression (4.1) of Estabrook et al. (2000), while the dashed line plots the spectrum of *Synthetic LISA*'s pseudorandom time series. The agreement is excellent, except at frequencies $\simeq f_b$ (0.5 Hz), where the effects of linear interpolation and of the finite-difference filter become noticeable. [For both curves, the nulls at the armlength-travel frequencies k/L have finite depth, for

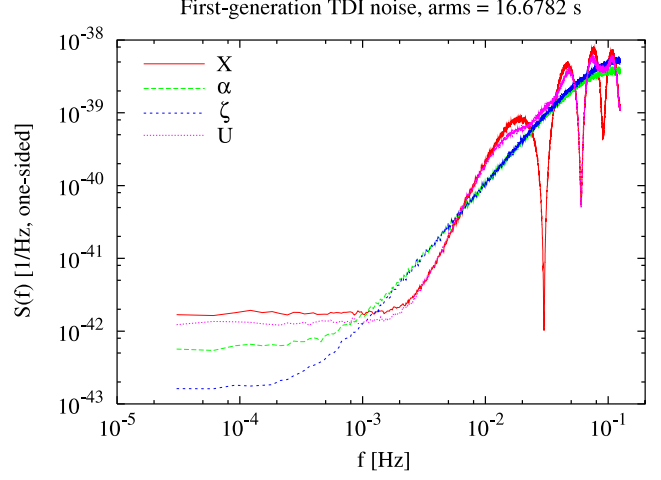


FIG. 14.—Spectral densities of the first-generation TDI observables X , α , ζ , and U , for a stationary, equal-arm interferometer with $L_i = 16.6782$ s. Compare with Fig. 1 of Armstrong et al. (2003). The spectra are suppressed at high frequencies by the effects of linear noise interpolation and of the finite-difference time-domain filter. The spectra were produced by the *Synthetic LISA* example script `test-tdiequal`.

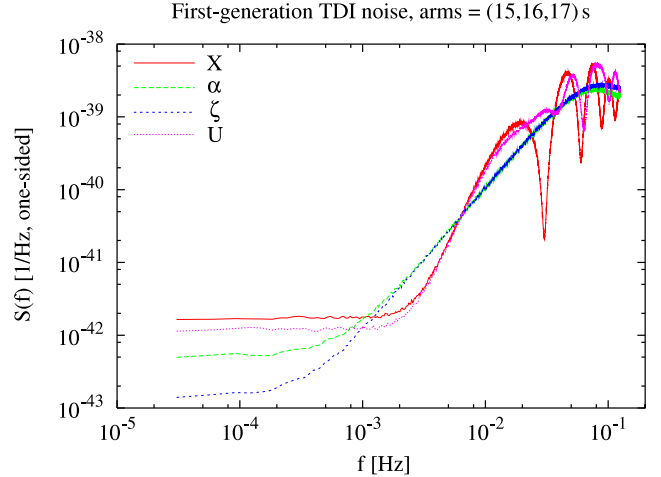


FIG. 15.—Spectral densities of the first-generation TDI observables X , α , ζ , and U , for a stationary, unequal-arm interferometer with $L_1 = 15$ s, $L_2 = 16$ s, $L_3 = 17$ s. Compare with Fig. 14. The spectrum was produced by the *Synthetic LISA* example script `test-tdiunequal`.

two different reasons: for the analytical expression, because the finite set of frequencies used to plot the curve does not include k/L ; for the *Synthetic LISA* time series, because of spectral leakage.]

Figure 14 compares the spectra of various first-generation TDI observables, again for an equal-arm configuration: this plot compares favorably with Fig. 1 of Armstrong et al. (2003). The reader might be puzzled by the flatness of the noise curves at low frequencies, as compared to the f^{-2} low-frequency dependence of proof-mass noise, and to the f^{-1} dependence of the often-seen LISA *sensitivity curves* (such as those produced by the online *LISA Sensitivity Curve Generator*).

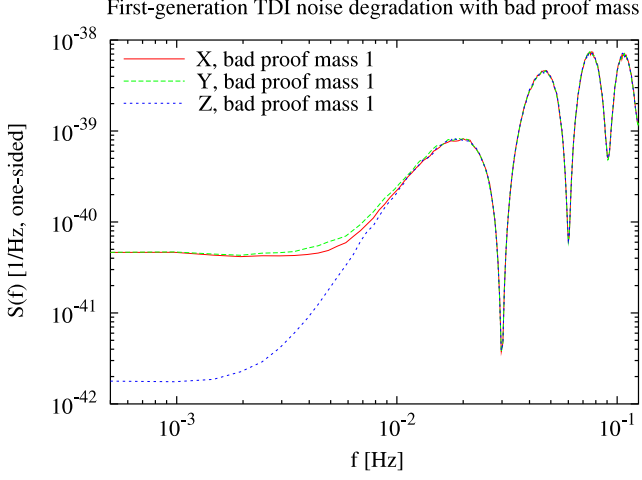


FIG. 16.— Spectral density of the first-generation TDI observables X , Y , and Z in a stationary, equal-arm interferometer with $L = 16.6782$ s, for standard noises (solid), and for $\times 10$ noise in proof mass 1. The spectra were produced by the *Synthetic LISA* example script `test-tdibadmass`.

tor¹⁴). The flatness is caused by the time-delay structure of first-generation TDI observables, which contain, as it were, a finite-difference time derivative with low-frequency power transfer function proportional to f^2 . As for the sensitivity curves, these always plot a ratio of noise response to (rms) GW-signal response; since the same transfer function applies to the GW signal as well as to the secondary noises, at low frequencies the sensitivity curves must rise (to higher strain for the same S/N) as the GW-signal response decreases.

In producing both Figs. 13 and 14 (and generally for all the spectra shown in this paper, except where otherwise specified), laser frequency noise at the standard nominal level of 1.1×10^{-26} Hz⁻¹ was explicitly included in the simulation; thus, these plots confirm that for stationary LISA configurations the first-generation TDI observables cancel frequency laser noise to the level of the secondary noises, and by up to 160 dB. In fact, if we were to show the spectra of the basic y_{slr} measurements, these would appear in these figures as straight lines at the 10^{-26} Hz⁻¹ level. Prior to this work, laser-noise cancellation had been simulated explicitly only by setting the LISA armlength to a multiple of the sampling time (Vallisneri & Armstrong 2003), which removes the need to interpolate noise. Of course, the simulation of laser-noise cancellation is much more interesting for realistic LISA geometries that include the rotation and flexing of the array: such tests are presented in the next section.

Last, Figs. 15 and 16 are meant to exemplify the ease with which *Synthetic LISA* can probe the effects of modified LISA configurations. Figure 15 shows noise spectra for the first-generation TDI observables in a stationary, *unequal-arm* interferometer: observe the resulting distortion of the noise curves with respect to Fig. 14. Figure 16 shows X , Y , and Z noise spectra for bad ($\times 10$ rms) noise in proof mass 1; in this example, first shown by Armstrong et al. (2003), the comparison of the three

¹⁴ Larson, S. L., *LISA Sensitivity Curve Generator*: www.srl.caltech.edu/shane/sensitivity.

eight-pulse TDI observables pinpoints the origin of the excess noise to the faulty proof mass.

4.4. TDI cancellation of laser noise

As recognized by Cornish & Hellings (2003), the eccentric and inclined orbital motion of the LISA spacecraft introduces a time variation in the armlengths of order 10^{-8} s/s, given approximately by Eq. (24); consequently, the first-generation and modified TDI observables discussed in Sec. 2.4 fail to cancel laser frequency noise completely. Graphically, we would see that the interferometric circuits synthesized by the observables fail to close exactly: the laser-noise residuals arise from the starting points of the paths, and they are of the form

$$\delta C_i = \frac{1}{2}[C_{i;J}^*(t) - C_{i;I}^*(t)] - \frac{1}{2}[C_{i;I}(t) - C_{i;J}(t)] \quad (31)$$

$$\simeq \frac{1}{2}[\dot{C}_i^*(t) + \dot{C}_i(t)](t_{;J} - t_{;I}) = \frac{1}{2}[\dot{C}_i^*(t) + \dot{C}_i(t)]\delta t,$$

where I and J denote ordered path retardation chains. Using the Fourier derivative theorem and assuming white uncorrelated laser noises, we get

$$|\delta \tilde{C}_i(f)|^2 / |\tilde{C}_i|^2 = 2\pi^2 f^2 \delta t^2, \quad (32)$$

for frequencies up to the laser-noise bandlimit. For the modified TDI X observable,¹⁵ $\delta t \simeq 10^{-6}$ s, so laser noise is canceled by less than 160 dB for $f \gtrsim 2$ mHz; for the second-generation TDI X_1 observable, $\delta t \simeq 10^{-10}$ s, so laser noise is canceled comfortably by more than 160 dB throughout the LISA band of good sensitivity. In the rest of this section, we discuss the results of *Synthetic LISA* simulations carried out to investigate (and substantiate) these analytic arguments.

Figure 17 shows the spectrum of secondary noise plus residual laser noise (long-dashed) versus the spectrum of secondary noise alone (solid) for the modified TDI X observable, with realistic eccentric and inclined LISA spacecraft orbits; the excess noise is evident between 1 mHz and 10 mHz, and within the noise nulls at frequency multiples of $1/(2L)$. The intermediate curves (short-dashed and dotted) show the effect of reducing the laser noise to respectively 0.3 and 0.1 times its nominal rms spectral density 1.1×10^{-26} Hz⁻¹.

Figure 18 shows the reduction caused by the residual laser noise in the (amplitude) S/N for monochromatic sources, computed with respect to the hypothetical case of perfect cancellation. The loss of sensitivity appears significant (up to $\sim 30\%$) between 1 mHz and 10 mHz, and even more so around $f = k/(2L)$. However, an improvement in laser noise stability by a factor of about three would be sufficient to erase the S/N-reduction bump at lower frequencies, and to shrink considerably the S/N-reduction peaks at higher frequencies. An improvement by a factor of ten would essentially eliminate the need for second-generation TDI, as estimated analytically by Cornish & Hellings (2003).

By contrast, Fig. 19 shows that perfect laser-noise cancellation is achieved with the second-generation TDI observable X_1 . Figure 20, the last in this line of investigation, examines imperfect laser-noise cancellation with

¹⁵ This can be tested using *Synthetic LISA*'s function `retardation(lisa, r1, ..., rs, t) = t_{;{r_i}}` (see Tab. A2) with $\{r_i\} = \{2, -2, -3, 3, 0, 0, 0, 0\}$ and $\{-3, 2, 2, -2, 0, 0, 0, 0\}$ (for X) and $\{r_i\} = \{2, -2, -3, 3, -3, 3, 2, -2\}$ and $\{-3, 3, 2, -2, 2, -2, -3, 3\}$ (for X_1).

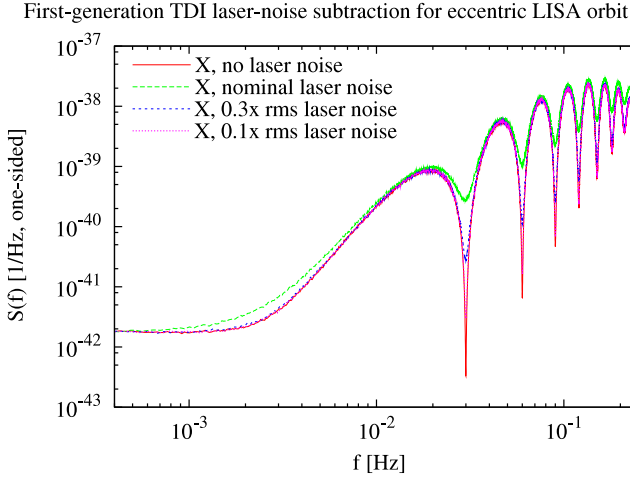


FIG. 17.— Imperfect cancellation of noise with modified TDI X for flexing LISA array (`EccentricInclined`, $\xi_0 = \eta_0 = 0$). The continuous curve shows the perfect-cancellation noise target, obtained by setting the laser noise to zero; the long-dashed, short-dashed, and dotted curves show the noise spectra resulting from imperfect laser-noise cancellation, for respectively nominal, 0.3× rms, and 0.1× rms laser noise. The spectra were produced by the Synthetic LISA example script `test-tdi2nd`.

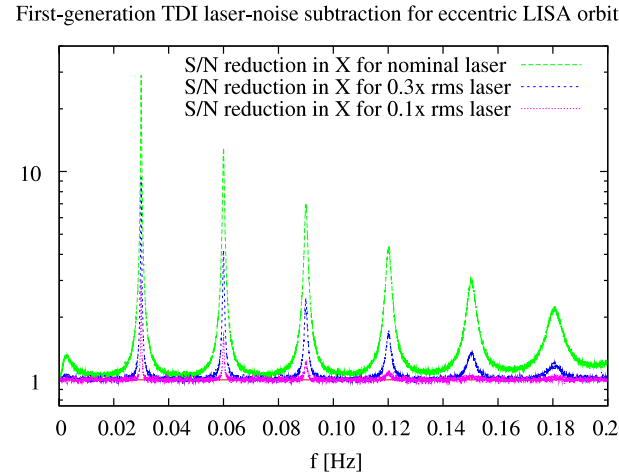


FIG. 18.— Reduction in amplitude S/N due to imperfect laser-noise cancellation for modified TDI X , with realistic LISA space-craft orbits (`EccentricInclined`, $\xi_0 = \eta_0 = 0$) and with nominal laser noise (long-dashed), 0.3× rms laser noise (short-dashed), and 0.1× rms laser noise (dotted). Because of the linear frequency axis used in this graph, the bump between 1 mHz and 10 mHz (which tops at about 1.3) appears unimpressive, but it spans a scientifically important frequency range. The TDI spectra were produced by the Synthetic LISA example script `test-tdi2nd`.

first-generation TDI when LISA is operated by locking all the lasers to a master (Tinto et al. 2003). Somewhat surprisingly, the spectrum of secondary noise plus residual laser noise is a factor of two higher for phase-locked operation (short-dashed curve) than for nonlocked operation (long-dashed curve); a tenfold (rms) reduction in laser-noise (dotted curve) would still be sufficient to essentially eliminate the need for second-generation TDI. Although this increase in residual noise under phase locking is, as far as we know, a novel result, it is explained easily by looking at Eq. (31): under locking, the two laser noises

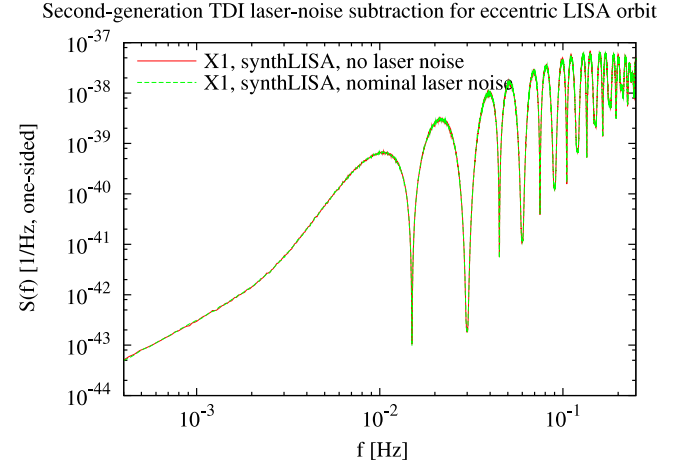


FIG. 19.— Perfect cancellation of laser noise with second-generation TDI X_1 for flexing LISA array (`EccentricInclined`, $\xi_0 = \eta_0 = 0$). The noise spectrum obtained by including nominal laser noise (dashed) matches the perfect-cancellation noise target obtained by setting the laser noise to zero (continuous). The spectra were produced by the Synthetic LISA example script `test-tdi2nd`.

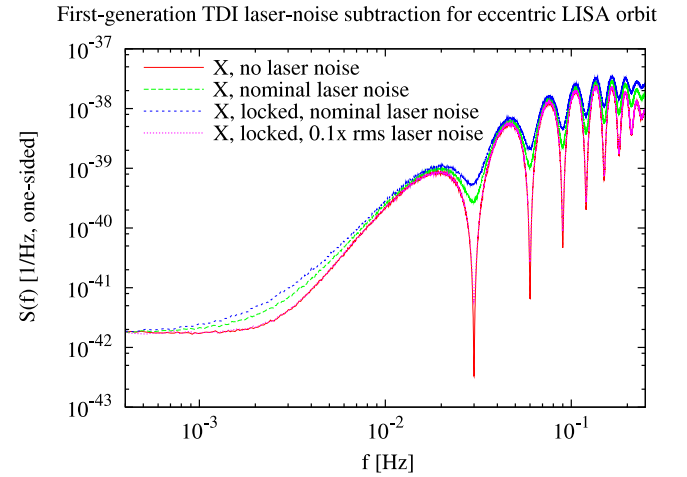


FIG. 20.— Imperfect cancellation of noise with modified TDI X for flexing LISA array (`EccentricInclined`, $\xi_0 = \eta_0 = 0$), and for phase-locked lasers. The continuous curve shows the perfect-cancellation noise target, obtained by setting the laser noise to zero; the long-dashed, short-dashed, and dotted curves show the noise spectra for nominal laser noise and no locking, nominal laser noise and phase-locked operation, and 0.1× rms laser noise and phase-locked operation.

$C_i(t)$ and $C_i^*(t)$ become almost perfectly correlated, so the right-hand side of Eq. (32) must be multiplied by a factor of two.

We now turn to simulating the laser-noise residuals resulting from the implementation of TDI using an imperfect knowledge of the armlengths, and therefore of the TDI delays. In this case, residuals are created at all the delayed times that appear in the TDI observables, and not just at the starting point of the interferometric circuits. Graphically, the reason is that the tail of each y_{slr} arrow (determined by a *physical* light-travel delay) does not precisely match the head of the preceding arrow (determined by a *nominal* TDI delay affected by

armlength-measurement error). At each such point, the residual has the form

$$\delta C_s \simeq \dot{C}_s(t) \delta L_l(t); \quad (33)$$

the total residual noise is a somewhat complicated function of the TDI observable under consideration, since residuals from the same laser may come in at different times, bringing in noise correlations.

During the LISA mission, arm lengths will probably be determined by means of an orbital-dynamics model that is periodically updated by ranging measurements, either between the spacecraft, or to Earth. Tinto et al. (2003) find that an arm length accuracy of ~ 30 m (~ 100 ns) would be needed for effective laser-noise subtraction with first-generation TDI. They also estimate how often the arm length measurements would need to be updated, by computing the timescale for the time-dependent arm lengths to change by an amount equal to the accuracy; for realistic orbits, this timescale varies substantially through the year, but it can be as low as 10 s. In our simulations we assume that new measurements are made approximately every light-travel time (~ 17 s), and we model the errors on the six (oriented) arm lengths as uncorrelated, white, Gaussian additive noises, bandlimited at $f_b = 1/(2L)$, with variance equal to a fraction of the nominal arm length accuracy.¹⁶

Figure 21 shows that with first-generation TDI it is enough to set the arm length-measurement noise 3- σ level to 50 m (short-dashed curve) to bring the residual laser noise down to the level caused by imperfect cancellation with time-dependent arm lengths and nominal laser noise (continuous curve). This result confirms the analytical estimate given by Tinto et al. (2003). Our simulations suggest also that arm length-measurement requirements are rather more stringent for second-generation TDI, at least for frequencies below 10^{-3} Hz: from Fig. 22 it appears that the 3- σ noise level must be less than 5 m to achieve the perfect-cancellation target.

These tests conclude our investigations of noise profiles and laser-noise cancellation for first- and second-generation TDI observables. We now move on to GW signals.

4.5. GW signals

Synthetic LISA can synthesize the TDI responses to arbitrary GW sources,¹⁷ either by interpolating user-provided h_+ and h_\times time series (using the `Wave` class `InterpolateMemory`), or by incorporating custom-coded `Wave` classes (see Tab. A3). The first approach was used by the author in a study (Gair et al. 2004; LIST WG1 EMRI taskforce 2003) of detection prospects for the GW signals from compact stellar objects inspiraling into the supermassive black holes at the centers of galaxies: time series for h_+ and h_\times were produced using the Glampedakis-Hughes-Kennerick quasidiabatic orbit integrator (Glampedakis et al. 2002), and then fed to *Synthetic LISA*, which computed the corresponding

¹⁶ In *Synthetic LISA*, noisy arm lengths are obtained with the LISA derived class `NoisyLISA(basicLISA, ΔtL, SL)`, whereby white noise generated at time intervals Δt^L , with one-sided power spectral density S^L , is added to the arm lengths determined from the LISA object `basicLISA` (see Tab. A2).

¹⁷ As long as they can be written as superpositions of plane waves with definite propagation vectors.

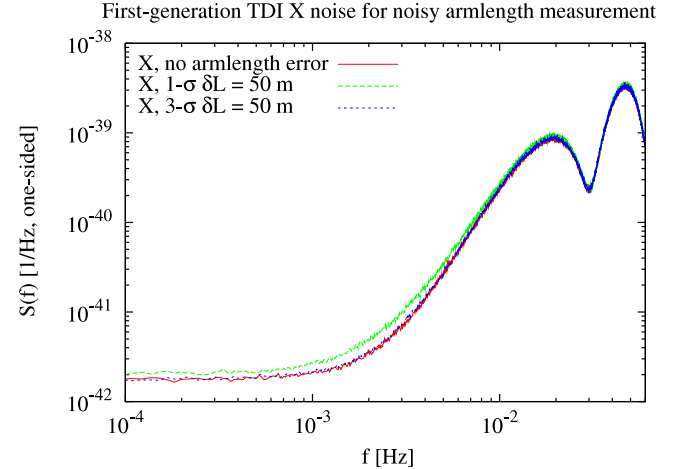


FIG. 21.— Imperfect cancellation of laser noise with modified TDI X due to imperfect knowledge of the arm lengths. The continuous curve shows the result of setting arm length-measurement noise to zero, as given by the secondary noises plus the residual laser noise due to using modified TDI with a flexing LISA array (thus, the continuous curve is identical to the long-dashed curve of Fig. 17); the long-dashed and short-dashed curves show the result of setting the arm length-measurement noise to, respectively, 1- σ and 3- σ levels of 50 m. The spectra were produced by the Synthetic LISA example script `test-noisyarms`.

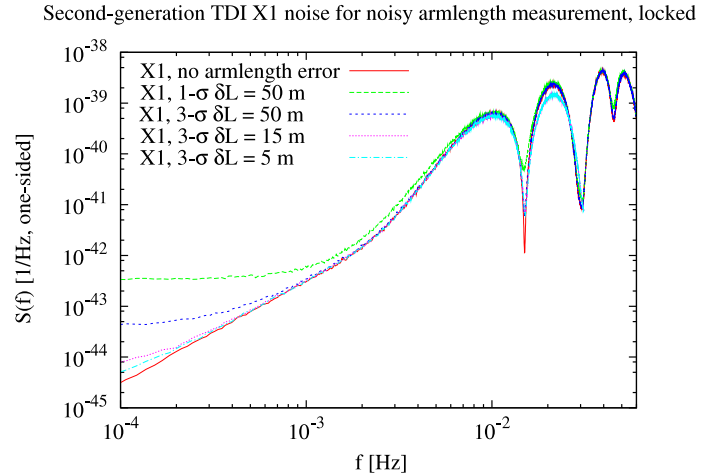


FIG. 22.— Imperfect cancellation of laser noise with second-generation TDI X_1 due to imperfect knowledge of the arm lengths. The continuous curve shows the result of setting arm length-measurement noise to zero, as given by the secondary noises alone; the long-dashed curve shows the result of setting the noise to a 1- σ level of 50 m; the short-dashed, dotted, and dash-dotted curves show the result of setting the noise to 3- σ levels of, respectively, 50 m, 15 m, and 5 m. The spectra were produced by the Synthetic LISA example script `test-noisyarms-2nd`.

time series of TDI observables; these were used to derive the expected S/Ns for the capture sources.

In this paper we limit our tests to GW signals from monochromatic binary sources, which already demonstrate the full effects of frequency and amplitude modulation (see Sec. 2.1), and for which accurate analytical expressions are available (Królak et al. 2004).

In the following, we characterize the closeness of two signals $s_1(t)$ and $s_2(t)$ by computing (one minus) the

normalized correlation product¹⁸

$$\frac{\int s_1(t)s_2(t) dt}{\int |s_1(t)|^2 dt}. \quad (34)$$

Królak et al. (2004) give analytical expressions valid at all frequencies for the GW responses of the first- and second-generation TDI variables; these expressions were obtained using the same approximated LISA orbits as implemented in the LISA class `CircularRotating` (see Sec. 3.2), but disregarding the causal laser-beam *look-ahead* implicit in Eq. (3), so that all six $L_l(t)$ stay equal and constant. Multiple checks conducted for monochromatic binaries with several GW frequencies between 10^{-4} and 10^{-1} , and with several random values of source latitude, longitude, and polarization, show that the TDI responses computed by *Synthetic LISA* (with `CircularRotating`) always match the theoretical expressions of Królak et al. (2004) to a few parts in 10^4 [i.e., Eq. (34) is of order one minus a few 10^{-4}].

Running *Synthetic LISA* with the more realistic LISA orbits implemented in `EccentricInclined`, the matching to the theoretical expressions of Królak et al. (2004) is still equally good at low frequencies, but the error grows to a few parts in 10^3 at $f \simeq 10^{-2}$ Hz, and to one percent or more at $f \simeq 10^{-1}$ Hz. These numbers characterize the accuracy of the approximation used by Królak et al. (2004) [see also Rubbo et al. (2003) for a discussion of the closely related *rigid adiabatic* approximation].

We have also found excellent agreement (see, e.g., Fig. 23) between the output of *Synthetic LISA* and the time series of TDI observables produced by the LISA Simulator, v. 2.0 (Cornish & Rubbo 2003).

5. THE FUTURE OF *SYNTHETIC LISA*

We have described the modeling and implementation of *Synthetic LISA*, a simulation of the LISA science process that can generate synthetic time series of fundamental noises and GW signals, as they appear in the laser-noise-cancelling TDI observables. We are making *Synthetic LISA* available¹⁹ as a public-domain software package to foster the involvement of the wider GW community in research on the interface between scientific goals and technical requirements for LISA, on tradeoffs and improvements for the implementation and operation of the mission, and on the development of novel data-analysis techniques for the LISA output. For this purpose, we have designed *Synthetic LISA* as a modular and easily extensible C++ package, with a user-friendly Python frontend for easy scripting and prototyping.

Synthetic LISA implements a full model of TDI, featuring time-dependent and causal armlengths, first- and second-generation TDI observables, and the explicit cancellation of laser noise. We have shown examples of *Synthetic LISA*'s usage, meant both as a validation of our model and as a realistic investigation of outstanding implementation issues: in particular, we have given the first quantitative estimate, based on a straight simulation, of

¹⁸ Note that the denominator of Eq. (34) contains the norm of only one of the two signals; thus, this correlation product is an index of amplitude matching as well as phase matching.

¹⁹ Open Channel Foundation: www.openchannelfoundation.org; for *Synthetic LISA* information and updates, see also www.vallis.org/syntheticlisa.

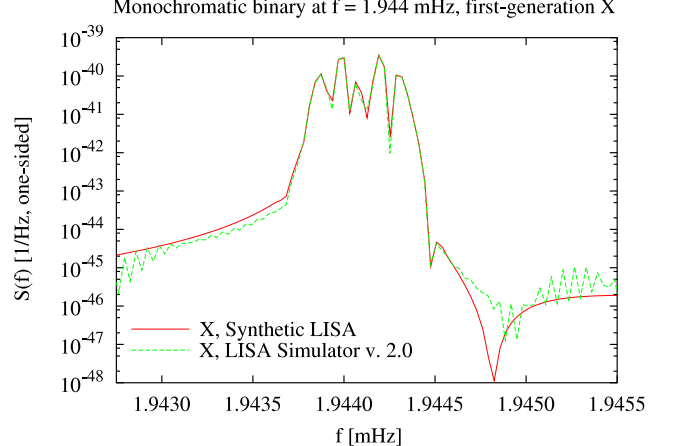


FIG. 23.— Comparison between the output of the LISA Simulator v. 2.0 (Cornish & Rubbo 2003) (continuous) and of *Synthetic LISA* (dashed) for the response of first-generation TDI X to a monochromatic binary with $f = 1.944$ mHz, $\beta = \lambda = \psi = 0$, $\iota \simeq \pi/2$, and amplitude appropriate for a $(0.5 + 0.033)M_\odot$ binary at 0.1 kpc. We show the nonaveraged spectra of the unwindowsed signals in a neighborhood of the central frequency. The mild jaggedness seen in the LISA Simulator signal is probably due to the linear-interpolation procedure used to approximate the GW strains h_+ and h_\times between sampled times. These spectra were produced by the *Synthetic LISA* example script `test-binary`.

To compare the fractional-frequency-fluctuation output of *Synthetic LISA* to the nominal-strain output of the LISA Simulator, we have multiplied the strain spectrum by square of the nominal armlength (10^{10} m) to get a displacement spectrum; converted to a velocity spectrum using the derivative theorem for Fourier transforms; and converted to a fractional-frequency-fluctuation spectrum by dividing by c^2 .

the improvement in laser-noise stabilization that would eliminate the need for second-generation TDI; we have shown that phase-locking of the lasers to a master would increase laser-noise residuals with first-generation TDI; and we have evaluated the armlength-measurement error budgets that would be required for effective laser-noise cancellation in first- and second-generation TDI.

The structure and programming style used for *Synthetic LISA* allows for vast extensions and improvements. Among others, we plan to include explicitly the additional time series required for calibration of the onboard ultrastable oscillators (Tinto et al. 2002), and to model measurement and quantization errors at the photodetectors. In the spirit of open-source design, we expect more useful additions, such as more realistic models of the noises and of the spacecraft subsystems, and additional Wave source modules, to come from the LISA and GW communities. GW data analysts using *Synthetic LISA* to generate simulated LISA data will also be able to exploit the library of GW signals being assembled at the *Mock LISA data archive*.²⁰

M.V. wishes to thank John Armstrong, Frank Estabrook, and Massimo Tinto for teaching him about all things TDI; and also Tom Prince, Bonny Schumaker, Andrzej Królak, Jeff Edlund, Daniel Shaddock, Bob Spero, Brent Ware, and Neil Cornish for useful discussions and

²⁰ Mock LISA Data Archive: astrograv.gsfc.nasa.gov/docs/mlda

interactions. John Armstrong developed precursor software to *Synthetic LISA* and assisted the development and testing of the current version, while Jeff Edlund provided help with coding. This research was supported by the LISA Mission Science Office at the Jet Propulsion Lab-

oratory, California Institute of Technology, where it was performed under contract with the National Aeronautics and Space Administration.

APPENDIX

SYNTHETIC LISA USAGE REFERENCE

Tables A2–A5 specify the syntax of the class constructors used to create the *Synthetic LISA* array-geometry (LISA), GW (Wave), fundamental-noise (Noise), and TDI (TDI) objects. In C++, these constructors can be used as shown in class declarations (“`OriginalLISA lisa(16,16,16);`”) or in the `new` construct (“`LISA *plisa = new OriginalLISA(16,16,16);`”); in Python, they are called directly to return a class reference (“`lisa = OriginalLISA(16,16,16)`”). Tables A2–A5 also describe the class methods available in C++ and Python, which can be accessed in both languages using the standard `class.method()` syntax (“`L = lisa.armlength(0)`”). [Under the hood, the *Synthetic LISA* C++ calls are interfaced to Python by wrappers generated automatically by SWIG.²¹ C++ arrays are mapped to Numeric²² array objects in Python.] Additional methods are available from C++, but they are likely to change in future versions of *Synthetic LISA* and should not be considered part of the standard package interface.

In the following, a **fixed-length font** indicates C++/Python methods and objects; by contrast, except where otherwise indicated, the arguments given in *italics* or as Greek letters are either integer indexes (C++ `ints`) or real quantities (C++ `doubles`). When function parameters are indicated with a default value (“`CircularRotating($\eta_0 = 0, \xi_0 = 0, sw = 1, t_0 = 0$)`”), they can be omitted, starting from the right, according to C++ custom.

TABLE A2 LISA OBJECTS

CONSTRUCTORS		
<code>OriginalLISA(L₁,L₂,L₃)</code>	L_1, L_2, L_3 [s]:	armlengths
<code>ModifiedLISA(L₁,L₂,L₃)</code>	L_1, L_2, L_3 [s]:	armlengths
<code>CircularRotating(L,η₀,ξ₀,sw,t₀),</code> <code>CircularRotating(η₀ = 0,ξ₀ = 0,sw = 1,t₀ = 0)</code>	L [s]: η_0 [rad]: ξ_0 [rad]: sw : t_0 [s]:	common armlength before aberration; set to 16.6782 s in the second form of the constructor true anomaly of LISA guiding center at $t = t_0$ initial phase of LISA array rotation at $t = t_0$ set positive (negative) value for clockwise (counterclockwise) s/c sequence 1 → 2 → 3 → 1 (as seen from $z > 0$) reference time for LISA orbital parameters (set to 0 implicitly in Sec. 3.2)
<code>EccentricInclined(η₀ = 0,ξ₀ = 0,sw = 0,t₀ = 0)</code>	η_0, ξ_0 [rad]: sw : t_0 [s]:	approximately as in <code>CircularRotating</code> see Sec. 3.2 for correspondence to the LISA Simulator (Cornish & Rubbo 2003) set negative to exchange spacecraft 2 and 3 reference time for LISA orbital parameters
<code>NoisyLISA(lisa,Δt,S_n)</code>	Δt [s]: S_n [1/Hz]:	returns a LISA object based on <code>lisa</code> , but with uncorrelated Gaussian, white noise processes perturbing the six nominal armlengths used to compute the TDI delays (but not the physical armlengths used to model laser-beam propagation) generation timestep of the pseudorandom armlength noise one-sided power spectral density of armlength noise
METHODS		
<code>armlength(arm,t)</code>		returns the light-propagation length $L_{arm}(t)$ (in seconds) experienced along <code>arm</code> for reception at time t (seconds); for <code>CircularRotating</code> and <code>EccentricInclined</code> , the armlength is approximated by Eqs. (21) and Eq. (24), respectively
<code>putp(p,spacecraft,t)</code> [C++ only]		fills the <code>Vector</code> object <code>p</code> with the position of <code>spacecraft</code> (given in SSB ecliptic coordinates, in geometrized units of seconds) at time t (seconds)
<code>putn(n,arm,t)</code> [C++ only]		fills the <code>Vector</code> object <code>n</code> with the photon-propagation unit vector (in SSB ecliptic coordinate components) for transmission along <code>arm</code> and reception at time t (seconds)
<code>retardation(lisa,d₁,...,d₈,t)</code> [helper function]		returns the retarded time $t_{\{d_i\}}$ (seconds); to use fewer than eight delays, set $d_i = 0$ from the right

TABLE A3 WAVE OBJECTS

CONSTRUCTORS	
<code>InterpolateMemory(hparray,hcarray,samples,Δt,lookback,β,λ,ψ)</code>	<code>hparray, hcarray</code> : pointers to C double arrays (or references to Numeric ‘d’ arrays) containing the h_+ and h_\times sequences

²¹ SWIG website: www.swig.org.

²² Numerical Python project website: sourceforge.net/projects/numpy.

TABLE A3 WAVE OBJECTS, CONTINUED

	<i>samples</i> :	total number of samples in the h_+ and h_\times sequences
	Δt [s]:	time spacing of the samples
	<i>lookback</i> [s]:	displaces the time indexing of the arrays so that the n th elements correspond to the time ^a $t = n\Delta t - \text{lookback}$
	β, λ, ψ [rad]:	source ecliptic latitude, ecliptic longitude, and polarization angle; see Sec. 3.3 for correspondence to the LISA Simulator (Cornish & Rubbo 2003)
<code>SimpleBinary</code> ($f, \phi_0, \iota, A, \beta, \lambda, \psi$)	f [Hz]:	GW frequency, as observed in the SSB frame
	ϕ_0 [rad]:	phase at $t = 0$
	ι [rad]:	binary inclination angle
	A [strain]:	common h_+ and h_\times amplitude
	β, λ, ψ [rad]:	as in <code>InterpolateMemory</code>
User-defined Wave classes		<i>constructors</i> should call the base class constructor <code>Wave</code> (β, λ, ψ); the new class must define the methods <code>hp(t)</code> and <code>hc(t)</code> . Users might find it expedient to modify the code for <code>SimpleBinary</code> , found in the source file <code>lisasim-wave.cpp</code>
		METHODS
<code>hp(t), hc(t)</code>		return GW polarizations $h_+(t)$ and $h_\times(t)$ at time t (seconds)

^a This offset is inserted because the expressions for the TDI observables contain two kind of delays: the first kind corresponds to retarding (or advancing) the phase of the plane GW to the current position of the LISA array (for the baseline LISA orbit this offset can be up to R , or ~ 500 s, depending on \dot{k}); the second kind corresponds to displacing the basic Doppler observables by one or more armlengths, as required by the TDI observables (this offset can be up to $8 \times L \simeq 8 \times 16.7$ s, for second-generation TDI and for the baseline LISA array formation). Thus, computing the TDI responses to a GW at time $t = 0$ can involve the values of h_+ and h_\times at times as early as $t \simeq -635$ s, or as late as $t \simeq 500$ s. To compute the LISA response in the time interval $[0, T]$, the user should provide at least $1 + (T + 2R + 8L)/\Delta t$ samples [$\sim 1 + (T + 1135)$ s]/ Δt for the baseline LISA configuration], and set *lookback* to at least $(\Delta t + R + 8L)$.

TABLE A4 NOISE OBJECTS

		CONSTRUCTORS
<code>InterpolateNoise</code> (<i>noisearray</i> , <i>samples</i> , Δt , <i>prebuf</i> , <i>norm</i> , <i>filter</i> = 0, <i>wind</i> = 1)	<i>noisearray</i> :	pointer to a C <code>double</code> array (or reference to a <code>Numeric</code> 'd' array) containing the raw noise sequence
	<i>samples</i> :	total number of samples in the noise sequence
	Δt [s]:	time spacing of the samples
	<i>prebuf</i> [s]:	displaces the indexing of the array so that the n th element corresponds ^a to the time $t = n\Delta t - \text{prebuf}$ (with $n = 0, \dots, \text{samples} - 1$)
	<i>norm</i> :	multiples the raw noise sequence
	<i>filter</i> :	sets filtering of the raw noise sequence (-2.0: damped-integrator filter; 2.0: finite-difference filter; 0.0: no filtering)
	<i>wind</i> [> 1]:	sets semiwidth of the data window used in Lagrange interpolation (a value of 1 yields linear interpolation)
<code>InterpolateNoise</code> (Δt , <i>buf</i> , S_n , e_n , <i>wind</i> = 1)	Δt [s]:	time spacing of the pseudorandom samples at generation
	<i>buf</i> [s]:	sets the minimum internal buffering of the pseudorandom sequences: after the noise has been requested at time t , the earliest noise value guaranteed to be available will be at time ^b $t - \text{buf}$
	S_n, e_n :	sets the one-sided power spectral density of the pseudorandom noise to $S_n \times f^{e_n}$, where $e_n = -2.0, 0.0$, and 2.0 are currently implemented (S_n is given in units of Hz, Hz^{-1} , and Hz^{-3} , respectively)
	<i>wind</i> [> 1]:	sets semiwidth of the data window used in Lagrange interpolation (a value of 1 yields linear interpolation)
		METHODS
<code>noise(t)</code>		returns the filtered, normalized value of the noise at time t (seconds)
<code>reset()</code>		resets the <code>Noise</code> object to time $t = 0$ by resetting buffer counters or reseeding pseudorandom number generators

^a The offset is needed because the LISA noises enter the TDI observables with delays up to four (for first-generation TDI) or eight (for second-generation TDI) armlengths; thus, if the user will be computing the LISA noise response in the time interval $[0, T]$, they should provide at least $1 + (T + 8L)/|\Delta t|$ noise samples in each noise object ($\sim 1 + (T + 136)$ s) for the baseline LISA configuration).

^b Again, it should be set to $4L$ (for first-generation TDI) or $8L$ (for second-generation TDI).

TABLE A5 TDI OBJECTS

	CONSTRUCTORS
--	--------------

TABLE A5 TDI OBJECTS, CONTINUED

<code>TDIsignal(lisa, wave)</code>	<code>lisa:</code>	C++ pointer (or Python reference) to LISA geometry object used to compute GW responses
	<code>wave:</code>	C++ pointer (or Python reference) to GW object
<code>TDInoise(lisa, Δt^{pm}, S^{pm}, Δt^{op}, S^{op}, Δt^{ls}, S^{ls})</code>	<code>lisa:</code>	C++ pointer (or Python reference) to LISA geometry object used to compute noise responses
	$Δt^{pm}, Δt^{op}, Δt^{ls}$ [s]:	set the time spacings used to generate the 18 (six proof mass, six optical path, six laser) standard pseudorandom noises sequences (done internally with <code>InterpolateNoise</code> and <code>wind = 1</code>)
	S^{pm} [Hz]:	sets the one-sided power spectral density of the six proof-mass noises to $S^{pm} \times f^{-2}$
	S^{op} [Hz ⁻³]:	sets the one-sided power spectral density of the six optical-path noises to ^a $S^{op} \times f^2$
	S^{ls} [Hz ⁻¹]:	sets the one-sided power spectral density of the six laser frequency noises to S^{ls}
<code>TDInoise(lisa, Δt^{pm} [6], S^{pm} [6], Δt^{op} [6], S^{op} [6], Δt^{ls} [6], S^{ls}) [6]</code>		as above, but takes parameters as C double arrays (or Python sequences) to set the attributes of the six noises of each type separately; the ordering of the parameters corresponds to $\{pm_1, pm_1^*, pm_2, pm_2^*, pm_3, pm_3^*\}$, $\{y_{12}^{op}, y_{21}^{op}, y_{23}^{op}, y_{32}^{op}, y_{31}^{op}, y_{13}^{op}\}$, and $\{C_1, C_1^*, C_2, C_2^*, C_3, C_3^*\}$
<code>TDInoise(lisa, proofnoise[6], opnoise[6], lasernoise[6])</code>	<code>lisa:</code>	as above
	<code>proofnoise[6]:</code>	array of C++ pointers (or Python sequence of references) to six <code>Noise</code> objects used to provide $\{pm_1, pm_1^*, pm_2, pm_2^*, pm_3, pm_3^*\}$
	<code>opnoise[6]:</code>	array of C++ pointers (or Python sequence of references) to six <code>Noise</code> objects used to provide $\{y_{12}^{op}, y_{21}^{op}, y_{23}^{op}, y_{32}^{op}, y_{31}^{op}, y_{13}^{op}\}$
	<code>proofnoise[6]:</code>	array of C++ pointers (or Python sequence of references) to six <code>Noise</code> objects used to provide $\{C_1, C_1^*, C_2, C_2^*, C_3, C_3^*\}$
METHODS		
<code>y(s, l, r, d₁, d₂, ..., d₇, t)</code>		basic LISA inter-spacecraft Doppler response $y_{slr; d_1 \dots d_n}(t)$ [emission at spacecraft s , transmission through arm l , and reception at r , retarded by the armlengths d_n to d_1] at time t (seconds); to use fewer than seven delays, set $d_i = 0$ from the right ^b
<code>z(s, l, r, d₁, d₂, ..., d₈, t)</code>		basic LISA intra-spacecraft Doppler response $z_{str; d_1 \dots d_n}(t)$ [made on the same bench as y_{slr}] at time t (seconds); to use fewer than eight delays, set $d_i = 0$ from the right
<code>alpha(t), beta(t), gamma(t), zeta(t), X(t), Y(t), Z(t)</code> <code>P(t), E(t), U(t)</code>		return first-generation TDI observables $\alpha, \beta, \gamma, \zeta, X, Y, Z, P, E$, and U at time t (seconds), as defined by Armstrong et al. (1999) and Estabrook et al. (2000)
<code>alpha1(t), alpha2(t), alpha3(t), Xm(t), Ym(t), Zm(t)</code>		return the modified TDI observables $\alpha_1, \alpha_2, \alpha_3, X, Y, Z$, as defined ^c by Tinto et al. (2004) and Shaddock et al. (2003)
<code>X1(t), X2(t), and X3(t)</code>		return the second-generation TDI observables X_1, X_2 , and X_3 , as defined ^c by Shaddock et al. (2003) and Tinto et al. (2004)
<code>reset() [TDInoise only]</code>		resets all <code>Noise</code> objects used in <code>TDInoise</code>
<code>lock(master) [TDInoise only]</code>		phase-locks all six lasers to a master laser ($master = 1, 2, 3$ for $C_{1,2,3}$ and $master = -1, -2, -3$ for $C_{1,2,3}^*$); <code>Xmlock1(t)</code> , <code>Xmlock2(t)</code> , and <code>Xmlock3(t)</code> then provide simplified (two-way-one-way hybrid) TDI expressions (Tinto et al. 2003)
<code>stdproofnoise(lisa, Δt^{pn}, S^{pn}),</code> <code>stdopticalnoise(lisa, Δt^{op}, S^{op}),</code> <code>stdlasernoise(lisa, Δt^{ls}, S^{ls})</code> [helper functions]		return C++ pointers (or Python references) to pseudorandom <code>InterpolateNoise</code> objects with time spacings $Δt^{pn}$, $Δt^{op}$, and $Δt^{ls}$ and one-sided power spectral densities $S^{pn} \times f^{-2}$, $S^{op} \times f^2$, and S^{ls} ; the LISA object <code>lisa</code> is used to choose a sufficiently long noise buffer to accommodate second-generation TDI time delays

^a Since the finite-difference time-domain filter has a spectral transfer function proportional to $\sin^2(\pi f \Delta t^{op})$, the spectrum of the synthesized optical-path noise will only be accurately proportional to f^2 at relatively low frequency [with respect to the Nyquist frequency of noise generation $(2\Delta t^{op})^{-1}$]. Thus, this frequency should be set comfortably higher than the highest frequency at which one wishes to analyze the TDI noise responses, but lower than the Nyquist frequency used to sample the TDI observables, to avoid aliasing.

^b `TDIsignal` synthesizes the $y_{slr; d_1 \dots d_n}^{gw}(t)$ response as follows: (a) it computes the reception time $t_r = t_{d_1, \dots, d_n}$ by calling repeatedly the LISA method `armlength`, according to the retardation chain rule (16); (b) it determines the emission time $t_s = t_r - L_l(t_r)$ and the causal photon propagation vector $\hat{n}_l(t_r) \propto \vec{p}_r(t_r) - \vec{p}_s(t_s)$, by calling the LISA method `putn`; (c) it obtains the GW retardations $\hat{k} \cdot \vec{p}_s(t_s)$ and $\hat{k} \cdot \vec{p}_r(t_r)$, by calling the LISA method `putp` and accessing the `Vector` object `k` of the class `Wave` [Eq. (26)]; (d) it requests the gravitational tensors $\mathbf{h}[t_s - \hat{k} \cdot \vec{p}_s(t_s)]$ and $\mathbf{h}[t_r - \hat{k} \cdot \vec{p}_r(t_r)]$, by calling the `Wave` method `putwave` [Eq. (25)]; (e) it assembles the Doppler response according to Eq. (1).

^c In those references, primed link indices correspond in this paper to positive indices.

TABLE A5 TDI OBJECTS, CONTINUED

REFERENCES

Armstrong, J. W., Estabrook, F. B., & Tinto, M. 1999, *ApJ*, 527, 814

Armstrong, J. W., Estabrook, F. B., & Tinto, M. 2001, *Classical Quantum Gravity*, 18, 4059

Armstrong, J. W., Estabrook, F. B., & Tinto, M. 2003, *Classical Quantum Gravity*, 20, S283

Armstrong, J. W., Estabrook, F. B., & Wahlquist, H. D. 1987, *ApJ*, 318, 536

Armstrong, J. W., Iess, L., Tortora, P., & Bertotti, B. 2003b, *ApJ*, 599, 806

Ashby, N. 2003, *Living Rev. Relativity*, 6, 1; www.livingreviews.org/lrr-2003-1

Bertotti, B., Ambrosini, R., Armstrong, J. W., Asmar, S. W., Comoretto, G., Giampieri, G., Iess, L., Koyama, Y., Messeri, A., Vecchio, A., Wahlquist, H. D. 1995, *Astron. Astrophys.*, 296, 13

Box, G. E. P., & Muller, M. E. 1958, *Ann. Math. Stat.*, 29, 610

Cornish, N. J., & Hellings, R. W. 2003, *Classical Quantum Gravity*, 20, 4851

Cornish, N. J., & Larson, S. L. 2003, *Classical Quantum Gravity*, 20, S163

Cornish, N. J., & Rubbo, L. J. 2003, *Phys. Rev. D*, 67, 022001; erratum, 029905; see also LISA Simulator v. 2.0, www.physics.montana.edu/lisa

Dhurandhar, S. V., Nayak, K. R., & Vinet, J.-Y. 2002, *Phys. Rev. D*, 65, 102002

Estabrook, F. B., Tinto, M., & Armstrong, J. W. 2000, *Phys. Rev. D*, 62, 042002

Estabrook, F. B., & Wahlquist, H. D. 1975, *General Relativity Gravitation*, 6, 439

Folkner, W. M., Hechler, F., Sweetser, T. H., Vincent, M. A., & Bender, P. L. 1997, *Classical Quantum Gravity*, 14, 1543

Gair, J. R., Barack, L., Creighton, T., Cutler, C., Larson, S. L., Phinney, E. S., & Vallisneri, M. 2004, *Classical Quantum Gravity*, in print; preprint (gr-qc/0405137)

Glampedakis, K., Hughes, S. A., & Kennefick, D. 2002, *Phys. Rev. D*, 66, 064005

Hogan, C. J., & Bender, P. L. 2001, *Phys. Rev. D*, 64, 062002

Krölak, A., Tinto, M., & Vallisneri, M. 2004, *Phys. Rev. D*, 70, 022003

LISA Study Team 1998, *LISA: Laser Interferometer Space Antenna for the Detection and Observation of Gravitational Waves*, Pre-Phase A Report, (2nd ed.; Garching, Germany: Max Planck Institut für Quantenoptik).

LIST WG1 EMRI taskforce 2003, Estimates of detection rates for LISA capture sources, technical report for the LISA Science Team Working Group I, preprint (www.vallis.org/publications)

Luescher, M. 1994, *Comp. Phys. Comm.*, 79, 100

Merkowitz, S. M. 2003, *Classical Quantum Gravity*, 20, S255

Merkowitz, S. M., Conkey, S., Haile, W. B., Kelly, W. R., III, Peabody, H., & Dumont, P. J. 2004, *Classical Quantum Gravity*, 21, S603

Peterseim, M., Robertson, D. I., Danzmann, K., Welling, H., & Bender, P. 2000, *Adv. Space Res.*, 25, 1143

Press, W. H., Flannery, B. P., Teukolsky, S. A., & Vetterling, W. T. 1992, *Numerical Recipes in C* (2nd ed.; Cambridge, MA: Cambridge University Press)

Prince, T. A., Tinto, M., Larson, S. L., & Armstrong, J. W. 2002, *Phys. Rev. D*, 66, 122002

Rubbo, L. J., Cornish, N. J., & Poujade, O. 2003, *Phys. Rev. D*, 69, 082003

Shaddock, D. A. 2004, *Phys. Rev. D*, 69, 022001

Shaddock, D. A., Tinto, M., Estabrook, F. B., & Armstrong, J. W. 2003, *Phys. Rev. D*, 68, 061303

Shaddock, D. A., Ware, B., Spero, R. E., & Vallisneri, M. 2004, *Phys. Rev. D*, submitted; preprint (gr-qc/0406106)

Stroustrup, B. 2000, *The C++ Programming Language* (Reading, MA: Addison-Wesley)

Tinto, M. 2002, *Classical Quantum Gravity*, 19, 1767

Tinto, M., & Armstrong, J. W. 1999, *Phys. Rev. D*, 59, 102003

Tinto, M., Armstrong, J. W., & Estabrook, F. B. 2000, *Phys. Rev. D*, 63, 021101(R)

Tinto, M., Estabrook, F. B., & Armstrong, J. W. 2002, *Phys. Rev. D*, 65, 082003

Tinto, M., Estabrook, F. B., and Armstrong, J. W. 2002b, *Time Delay Interferometry White Paper*, LISA Mission Science Whitepaper (www.srl.caltech.edu/lisa)

Tinto, M., Estabrook, F. B., & Armstrong, J. W. 2004, *Phys. Rev. D*, 69, 082001

Tinto, M., Shaddock, D. A., Sylvestre, J., & Armstrong, J. W. 2003, *Phys. Rev. D*, 67, 122003

Vallisneri, M., & Armstrong, J. W. 2003, *Synthetic LISA: Simulating Time Delay Interferometry in a Model LISA*, LISA Mission Science Whitepaper, v. 1.0 (www.srl.caltech.edu/lisa/documents.html)

Wahlquist, H. D. 1987, *General Relativity Gravitation*, 19, 1101